


2

REPORT DOCUMENTATION PAGE

Form Approved
OMB No. 0704-0188

1a. RE U		AD-A260 118		1b. RESTRICTIVE MARKINGS	
2a. SE				3. DISTRIBUTION/AVAILABILITY OF REPORT Approved for public release, distribution unlimited	
2b. DE					
4. PERFORMING ORGANIZATION REPORT NUMBER(S) FMRL-TR7				5. MONITORING ORGANIZATION REPORT NUMBER(S)	
6a. NAME OF PERFORMING ORGANIZATION Florida A & M University Dept. of Mechanical Engineering		6b. OFFICE SYMBOL (if applicable)		7a. NAME OF MONITORING ORGANIZATION Air Force Office of Scientific Research Division of Aerospace Sciences	
6c. ADDRESS (City, State, and ZIP Code) P.O. Box 2175 Tallahassee, FL 32316-2175				7b. ADDRESS (City, State, and ZIP Code) Bolling AFB, Bldg. 410 Washington, DC 20332-6448	
8a. NAME OF FUNDING/SPONSORING ORGANIZATION		8b. OFFICE SYMBOL (if applicable) NA		9. PROCUREMENT INSTRUMENT IDENTIFICATION NUMBER F49620-89-C-0067	
8c. ADDRESS (City, State, and ZIP Code) AFOSR/NA Bolling AFB DC 20332-6448				10. SOURCE OF FUNDING NUMBERS PROGRAM ELEMENT NO. PROJECT NO. TASK NO. WORK UNIT ACCESSION NO. 61102F-2307 CS	
11. TITLE (Include Security Classification) Unsteady Flow Past a Pitching Airfoil at Moderately High Subsonic Free Stream Mach Numbers					
12. PERSONAL AUTHOR(S) A. Krothapalli, G. Buzyna, and L. Lourenco					
13a. TYPE OF REPORT FINAL		13b. TIME COVERED FROM 89/06/01 TO 92/05/31		14. DATE OF REPORT (Year, Month, Day) 92/10/26	
				15. PAGE COUNT 57	
16. SUPPLEMENTARY NOTATION					
17. COSATI CODES FIELD GROUP SUB-GROUP			18. SUBJECT TERMS (Continue on reverse if necessary and identify by block number) NACA 0012, airfoil, flow Velocity		
19. ABSTRACT (Continue on reverse if necessary and identify by block number) An experimental and computational investigation was carried out to study the flow past a NACA 0012 airfoil undergoing pitch up motion at free Mach numbers ranging 0.3 to 0.8. The flow velocity field was captured using PIV demonstrating the ability of the technique to characterize high speed separated flows. A companion computational study was conducted to assess the effect of wind tunnel walls on the dynamic stall process.					
20. DISTRIBUTION/AVAILABILITY OF ABSTRACT <input checked="" type="checkbox"/> UNCLASSIFIED/UNLIMITED <input type="checkbox"/> SAME AS RPT. <input type="checkbox"/> DTIC USERS				21. ABSTRACT SECURITY CLASSIFICATION	
22a. NAME OF RESPONSIBLE INDIVIDUAL D. FANT, Major, USAF		22b. TELEPHONE (Include Area Code) 202 767-0471		22c. OFFICE/SYMBOL NA	

DTIC
ELECTE
JAN 27 1993

**Unsteady Flow Past a Pitching Airfoil at
Moderately High Subsonic Free Stream Mach Numbers**

**A Final Report Submitted to
The Air Force Office of Scientific Research**

by

**The Department of Mechanical Engineering
FAMU/FSU College of Engineering
Florida State University
Tallahassee, FL**

for the period covering
June 1989 - May 1992

**Principal Investigator
Professor Anjaneyulu Krothapalli**

October 29, 1992

93-01499


Table of Contents

Introduction	1
Blow-Down Wind Tunnel	2
Particle Image Velocimetry	4
Results and Discussion	7
Conclusions	9
References	10
Appendix A (High Speed Airfoil Flipping Mechanism)	
Appendix B (A Hybrid Grid Approach to Study Dynamic Stall)	

Accession For	
NTIS CRA&I	<input checked="" type="checkbox"/>
DTIC TAB	<input type="checkbox"/>
Unannounced	<input type="checkbox"/>
Justification	
By	
Distribution /	
Availability Codes	
Dist	Avail and/or Special
A-1	

INTRODUCTION

High angle of attack maneuvers of fighter aircraft present unusual challenges in the areas of unsteady aerodynamics and controls. Current fighter aircraft maneuvers are generally limited to angles of attack below their maximum lift capability. This is primarily due to degrading aerodynamic lateral and directional characteristics and reduced control power at high angles of attack, often resulting in uncontrollable maneuvers. In order to broaden our understanding a number of experimental programs have been initiated to explore high angle of attack flight beyond stall. Most of the basic studies in the literature dealing with this subject are conducted at low speeds, thus not addressing the problem of the compressibility effects on the unsteady large scale separated flow that occurs when a wing undergoes a pitching motion.

A research program was initiated to carry out a basic experimental and numerical study of the flow past an airfoil pitching at constant rates at high subsonic free stream Mach numbers ($0.3 < M < 0.8$). The main features of the flow consists of unsteady separation followed by large scale vortical structures and shock waves. The focus of this effort is to understand the role of shocks on the unsteady separation, and the formation and growth of the large scale vortical motions.

In order to provide a detailed quantitative description of the complex flow, a new experimental technique, commonly known as Particle Image Velocimetry, was developed to provide a two-dimensional instantaneous velocity and vorticity fields with good accuracy. Such a technique has been successfully implemented for high subsonic separated flows, and will be discussed later.

A new blow-down wind tunnel facility was developed to provide free stream Mach numbers varying from 0.3 to 0.8. The test section of the facility was specially designed to accommodate the PIV measurement capability.

In the following, the details of the various aspects of the research program are described.

BLOW-DOWN WIND TUNNEL

Experiments conducted in our intermittent blow down wind tunnel facility and described in earlier reports indicated a need for several facility modifications. These modifications included increasing high pressure storage capability, improving performance of the control valve system, adding the capability of preheating the air, and increasing the size of the test section. The modified facility is described below.

The modified experimental facility has a larger test section and the upper limit of the test section Mach number has been increased to $M = 0.7$. In order to increase running time at the higher mass flow rate, an additional tank which could be operated in series or in parallel with the existing air supply was installed. A schematic diagram of the new wind tunnel circuit configuration is shown in figure 1. The existing air supply system, referred to as the primary system, consists of three tanks with a total volume of 164 cubic feet and piping limited to 0.7 inches internal diameter. The new system, referred to as the secondary system, consists of a single larger tank with a capacity of 170 cubic feet and a larger 1.69 inch internal diameter piping system. Both tanks operate at 2,000 psi. The facility can be operated with either tank system alone, or in series combination for larger flow rates.

In order to obtain finer flow control and avoid excess noise and vibration, both systems employ a two stage pressure regulation to reduce the extremely high storage pressure to the desired stagnation pressure. The old pressure regulators were retrofitted with new electronic controls and new, larger diameter, control valves are being acquired for the secondary air supply system. In each system, the first of the two pressure regulators reduces the pressure to 150 psi, and the other maintains the desired stagnation pressure. The supply systems can be operated independently or in parallel.

A 500 kW heating capability was added to the primary system to provide air at 150 psi and 1,000F. Preheating the air solves a troublesome condensation problem which interfered with our PIV measurement technique. The fine oil mist used to seed the air in previous experiments condensed on the inside of the windows and obstructed optical data acquisition. A similar obstruction was created by water condensation on the outside of the test section windows. Heated air from the primary system and cold air from the secondary system are mixed in a plenum to provide the desired stagnation temperature. The air supply can be seeded by injection into the plenum chamber, as shown in the schematic diagram, or by an injector upstream of the settling chamber. A solid particle seeding capability

is currently being designed and tested and will be implemented. This is shown in the schematic diagram.

The wind tunnel assembly, including the flow spreader, screens, settling chamber, nozzle and test section, is shown in greater detail in figure 2. The contraction section and nozzle have been redesigned to provide smooth flow for the larger, 6 in. x 6 in. test section. The modular test section is attached directly to the nozzle and allows wide latitude in the use of visualization and measuring techniques. The test section has provision for windows on all four sides to provide vertical sheet illumination and horizontal viewing. Since our experimental technique requires whole field measurements, it is imperative that the entire field be viewed and illuminated without any interference from the usual supported of airfoil models. Hence the model is supported directly by the side windows by means of pins which also allow for model rotation. The model airfoil is rotated by means of a spring-activated lever arm arrangement.

Running time as a function of Mach number for the modified tunnel is shown in figure 3. The limiting element for the system in the wind tunnel mode is the secondary air supply. Running time is adequate for the Mach numbers of interest shown., Except for temperature effects, the Reynolds number for a flow over a 3 cm chord air foil remains unchanged in the new tunnel. Reynolds number as a function of Mach number is shown in figure 4 for a 3 cm chord air foil and a stagnation temperature of 75F.

PARTICLE IMAGE VELOCIMETRY

Particle Image Velocimetry (PIV), a whole field velocity measurement technique, provides simultaneous visualization and quantification of the instantaneous two-dimensional velocity field in a selected plane of the flow field. The velocity field is obtained with sufficient accuracy and spatial resolution, the vorticity field can be easily calculated. This constitutes a great asset for the study of variety of flows that evolve stochastically in both space and time such as unsteady separated flows. The detailed description of the technique is given by Lourenco et al¹.

The application of PIV to the measurement of an instantaneous two-dimensional velocity field involves two basic steps. First it is necessary to illuminate the flow field with a thin laser light sheet; the flow is made visible through small tracer particles seeded in the fluid. The light scattered by the seeding particles, which follow the local fluid motion is recorded using a multiple exposure photograph or a high resolution CCD area sensor². The distance between the corresponding particle images being proportional to the displacement provides a measure of the local fluid velocity. To resolve the directional ambiguity of the velocity vector and to increase the dynamic range of the measurement, a velocity bias technique is implemented. This is accomplished by adding a uniform reference motion to the flow, thus superposing a velocity shift to the real flow field. A properly chosen shift can insure that all the image displacements occur in the same direction, thereby eliminating the directional ambiguity. The true flow field can be recovered later by removing the imposed shift from the raw velocity data.

Optical and digital image processing techniques are used to convert the particle image information into local velocity data. The optical process uses a focused low intensity laser beam to interrogate a small area of the multiple exposed photographic film. The diffraction pattern produced by the coherent illumination of the multiple images in the photographic transparency generates Young's fringes in the Fourier plane of a lens; if the multiple particle images within the interrogating area correlate. These fringes have an orientation that is perpendicular to the direction of the local displacement and a spacing inversely proportional to the displacement. A fully automated process has been devised to digitize and process the fringe images (see Ref. 1 for details). When using the digital image processing, an auto correlation approach is used for the evaluation of displacement of the particles. In this method, a small region containing particle image pairs is selected. A digital auto-correlation is computed and the corresponding of the

highest and second highest peaks, excluding the D.C peak placed at the origin, are found. Based on the acceptable signal to noise ratio (D.C peak amplitude vs the highest data peak amplitude) the measurement of the particle displacement is obtained. The detailed description of this approach is given by Lourenco et.al³.

A dual pulsed laser system, consisting of two Spectra-Physics DCR-11 Nd:Yag pulsed lasers, is used to provide the double illumination pulses. A system of prisms and polarizing cube beam combiners make the light beams emitted from the two lasers collinear. Time separation between the laser light pulses can be varied from 300 nsec to few seconds by adjusting a pulse generator used as a trigger. A cylindrical lens is used to form the combined beam into a laser sheet that illuminates the midspan section of the airfoil. The seeding consisted of micron sized smoke particles, from a Rosco smoke generator, introduced in the settling chamber of the wind tunnel by means of an ejector system. A 35mm Nikon F-3 camera with a 55mm macro lens is used to record the flow field.

A bias method using light polarization effect, proposed by Lourenco⁴, is used in the present experiments. A polarizing beam splitter cube and two quarter wave plate isolators arrangement as shown in figure 5 (a)-(c) is used. The quarter wave plates are coated with a totally reflective coating on the face away from the cube, and an antireflective coating on the surface closest to the cube. In figure 5(a) and 5(b) the light paths for the light scattered by a particle with p and s polarization states, are sketched. The principle of operation of the apparatus is as follows. Consider a stationary particle that is first illuminated by p-polarized light. The scattered beam travels through the cube undisturbed in its path and impinges onto the wave plate. The interaction between this beam and the wave plate results in a change in its state of polarization from p to s when it emerges from the 1/4 wave plate. The interaction involves first a change in polarization from linearly p-polarized to right circular, from right circular to left circular upon the total reflection at the wave plate surface away from the cube and from left circular to linearly s-polarized upon the second travel through the cube. The light ray with its state of polarization rotated by 90 degrees is reflected at the cube's interface and directed towards the camera objective. In contrast, if the light beam is initially linearly s-polarized, as shown in figure 5(b), it undergoes first the total reflection at the cube's interface, directed towards the other 1/4 wave plate where the state of polarization is changed to linear p-polarized, and proceeding through the cube and into the camera lens. Providing that the light paths for both p and s polarized beams are similar, and that the 1/4 wave plates are parallel to the cube's surfaces, the light rays will emerge at

the same location, and thus the particle image will be formed at the same point. A uniform displacement (shift) can be generated by slightly tilting one of the $1/4$ wave plates with respect to the cube's surface. The amount of variable separation between images is proportional to the angle of tilt (Figure 5(c)). Figure 6 shows the camera bias device assembly. Also shown in the picture is the airfoil in the test section.

RESULTS AND DISCUSSION

Two basic experiments were conducted to demonstrate the viability of PIV to measure separated and unsteady flows. The first experiment was conducted to obtain the instantaneous separated velocity field over a high angle of attack airfoil in steady free stream of $M=0.6$. Typical doubly exposed photographs of the flow, taken with the superposed velocity bias, at two different angles of attack are shown in figure 7. The NACA 0012 airfoil has a chord length of 3.8 cm. The airfoil has an aspect ratio of 4. The corresponding Reynolds number, based on the chord of the airfoil, is about 5×10^5 . These pictures clearly depict the separation region marked by the shear layers from the leading and trailing edges of the airfoil. The leading edge shear layer shows organized large scale vortical structures similar to those found in plane shear layers.

The film negatives were processed using the FFD Mark II Young's fringe analyzer to produce the flow fields of figure 8. In this figure the corresponding two dimensional velocity field is represented, upon removal of the uniform velocity bias, as uniformly scaled vectors (9600), shown in the laboratory reference frame. As it can be observed from figure 8 the present velocity bias device has made possible the detailed measurement of a fully separated high speed flow, which contained regions of stagnant and reversing flows with magnitude comparable to that of a free stream. Due to lack of seeding in some regions of the flow, drop out of the velocity vectors can be noticed. From the magnitude of the velocity vectors in the accelerated flow region near the leading edge, a region of supersonic flow is observed. Although, not observable in the smoke flow visualization pictures, it is possible that weak shock waves are present in the supersonic flow region, especially in the case of 30° angle of attack.

Experiments were also conducted at lower free stream Mach number of 0.3. Typical doubly exposed photographs of the flow, taken with the superposed velocity bias, at two different angles of attack are shown in figure 9. The corresponding velocity field is given in figure 10. The detailed structure of the separated flow can be clearly discerned from this type of data.

The ability of PIV to capture the unsteady separated flow is demonstrated by another experiment to study the detailed structure of the near wake of circular cylinder at $M=0.6$. The cylinder has a diameter of 1.27cm. The corresponding Reynolds number, based on the diameter of the

cylinder, is 143,000. Typical doubly exposed photographs of the flow, taken with the superposed velocity bias, at three different phases of a vortex shedding cycle are shown in figures 11. In figure 11a, the vortices appear almost symmetric with respect to the centerline. While, in figures 11b and 11c, they are out of phase (90°) with each other.

Figure 12 shows the corresponding two dimensional velocity fields, upon removal of the uniform velocity bias, as uniformly scaled vectors, shown in the laboratory reference frame. The corresponding out-of-plane vorticity fields are also shown in the figure. Following the time evolution of the instantaneous flow field, it is observed that there is a vigorous periodic flapping motion behind the cylinder. From the vorticity data, it is clear that the recirculation eddies consist of several smaller but individualized structures embedded in the shear layer. These secondary structures are generated due to the shear layer instabilities. It appears that these secondary eddies also undergo interactions in the form of vortex merging usually found in the mixing layers. The vortex formation process for low speed wakes seem to apply also for the high speed case. For instance, the shear layer from one side of the wake (upper shear layer in figure 12b) bends down and cuts off the supply of shear layer vorticity in to the developing vortex from the lower shear layer, initiating the shedding of a primary wake vortex. Secondly, it impedes the downstream convection of the lower shear layer vorticity, resulting local accumulation of the vorticity inside the recirculation region (Figure 12c). This local concentration of vorticity in the lower regions entrains a large amount of fluid from outside the wake, consequently, it bends the lower shear layer upward. This action leads to the later disengagement of a vortex from the upper shear layer, through a similar cut-off process as described above. This interaction alternates between the two shear layers and produces a periodic shedding of vortices of opposite sign behind the cylinder.

The above described experiments clearly demonstrate the ability of PIV to capture accurately the detailed velocity field in an unsteady separated flow. The corresponding vorticity field, which is essential in understanding these flows, can also be obtained with great accuracy. Based on these experiments, a detailed survey of the unsteady flow past a pitching airfoil is being conducted at this time. The results of that study will constitute a Ph.D dissertation of Mr. Billy Crisler.

CONCLUSIONS

A research program was initiated in 1989 to study the basic unsteady separated flow characteristics of a NACA 0012 airfoil undergoing pitch up motion at free stream Mach numbers ranging from 0.3 to 0.8.

A new blow-down wind tunnel facility has been built to investigate the present problem. The test section of the facility is designed to make the whole field non-intrusive measurements using Particle Image Velocimetry. A high speed airfoil pitching mechanism has also been built to provide high pitch rates.

The use of Particle Image Velocimetry to study high speed unsteady separated flows has been demonstrated by capturing the instantaneous separated flow over a high angle of attack airfoil at $M=0.6$. In addition, the time evolution of a unsteady near wake behind a circular cylinder at $M=0.6$ was also studied. These experiments clearly show that the PIV will enable us to measure the unsteady separated flow that occur on a pitching airfoil.

The experiments related to pitching airfoil are being conducted at this time and the results will be included in the Ph.D dissertation of Major Billy Crisler, who is expected to finish his studies by August 1993.

A companion computational study was conducted to assess the effect of wind tunnel walls on the dynamic stall process. An innovative hybrid grid approach was used to resolve the details of the dynamic stall vortex.

REFERENCES

1. Lourenco, L., Krothapalli, A., Smith C., " Particle Image Displacement Velocimetry and Laser Speckle Velocimetry" in Advances in Fluid Mechanics. Editor M. Gad-el-Hak, Springer-Verlag, 1989, pp 128-199
2. Lourenco, L., "Turbulence Measurements Using a 'On-Line' PIV" Paper presented at Third French Congress in Laser Velocimetry; Toulouse, 1992
3. Lourenco, L., Gogigeni, S., La Salle R., " 'On-Line' PIV: An Integrated Approach", submitted to Applied Optics
4. Lourenco, L. " A Velocity Bias Technique for PIV Measurements of High Speed Flows", to appear in Applied Optics

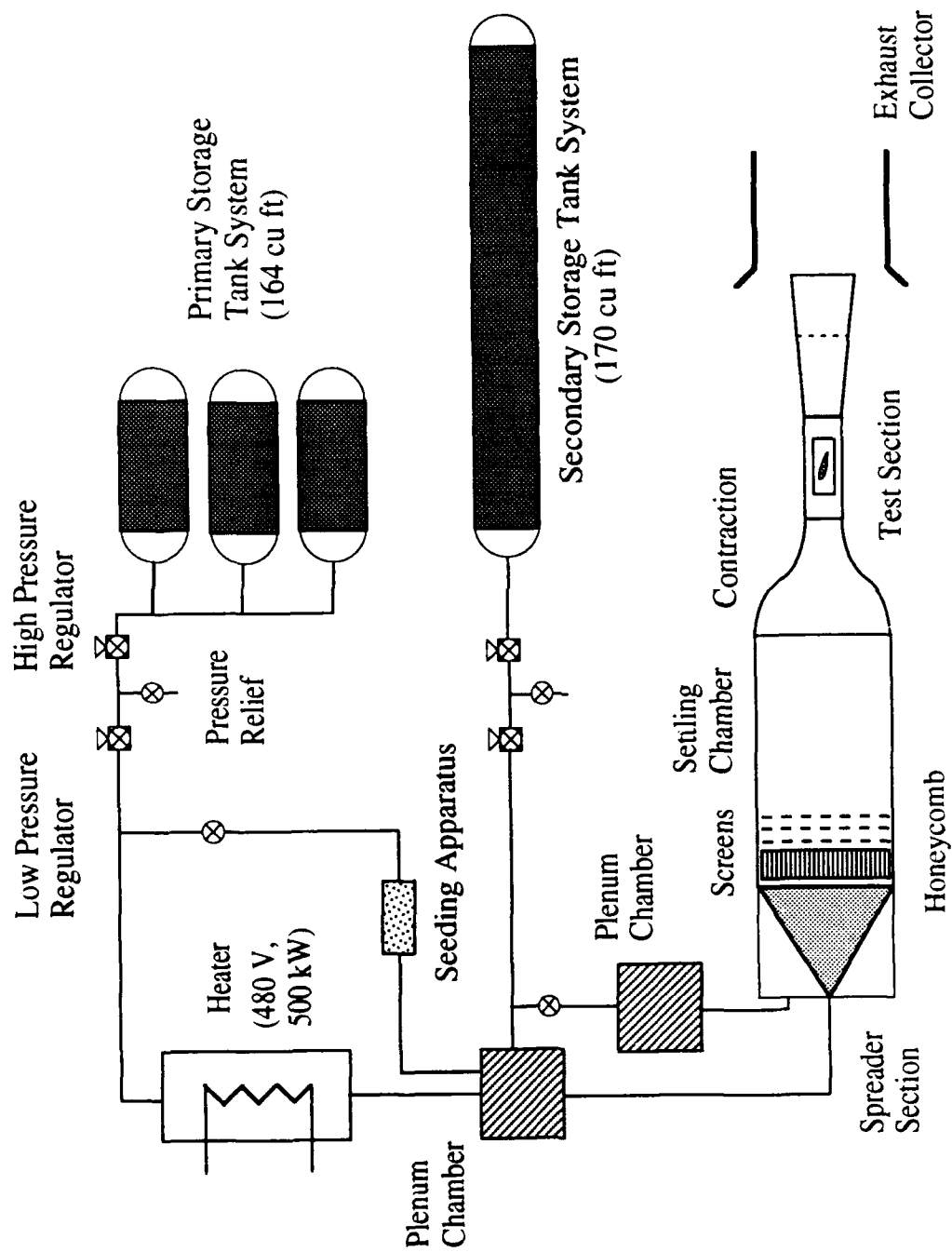
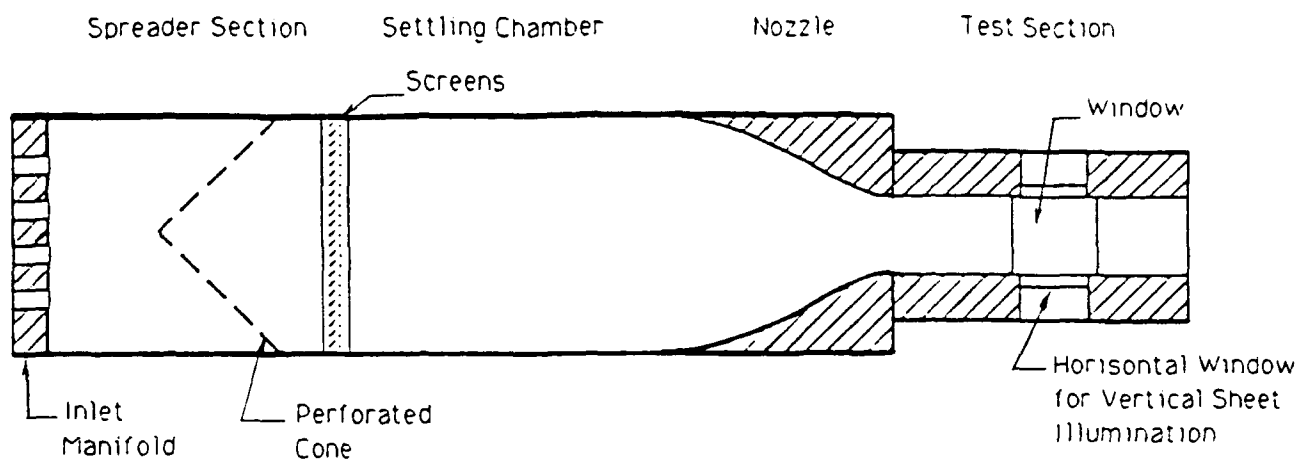


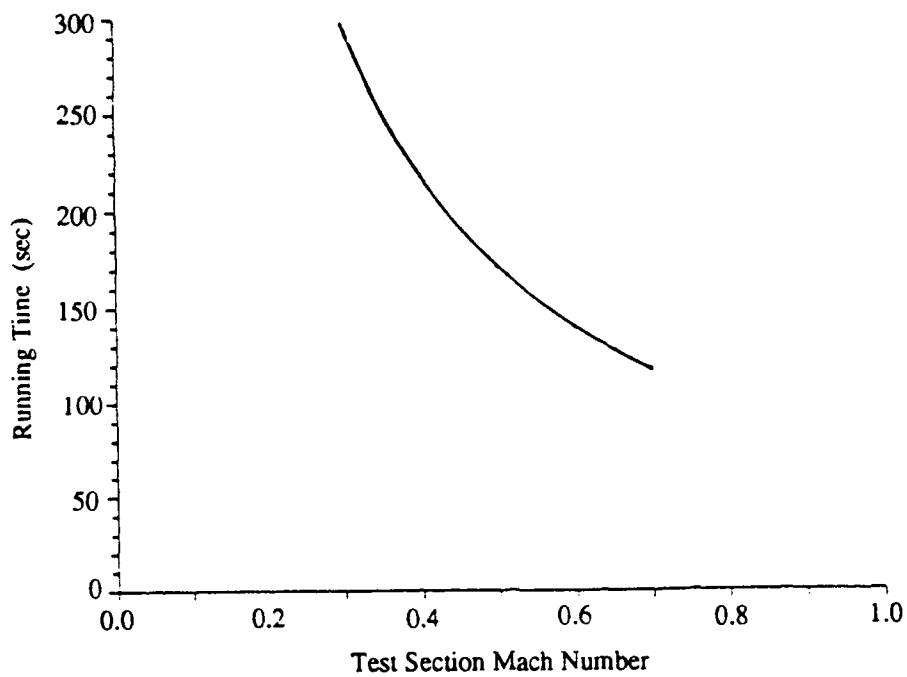
Figure 1

High-Speed Boltdown Wind Tunnel Facility



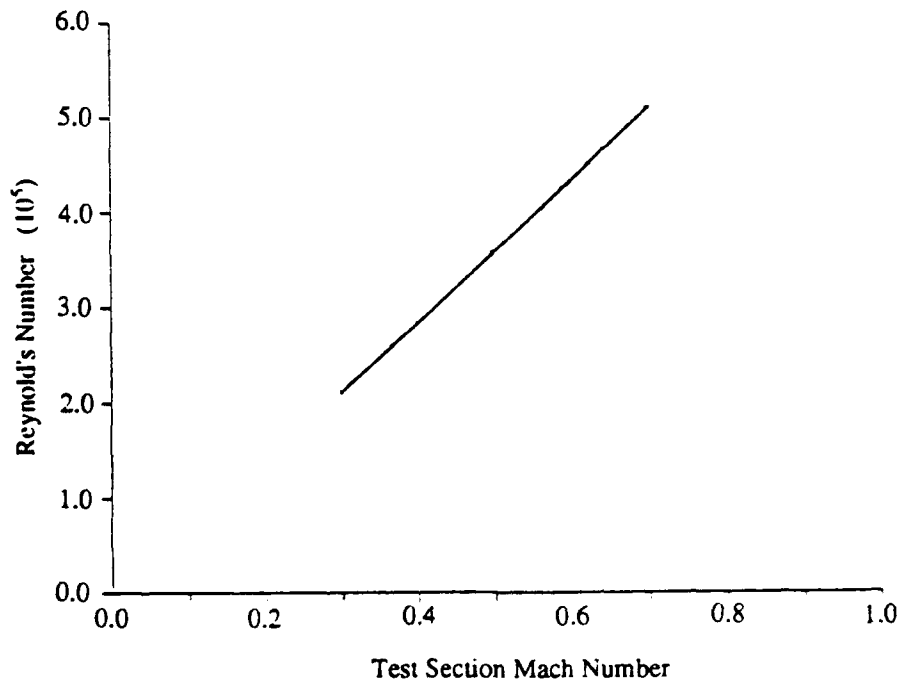
Flow Spreader, Settling Chamber, and
Nozzle Section of the Intermittent Wind Tunnel

Figure 2



Running Time as a Function of Test Section Mach Number

Figure 3



Reynolds Number as a Function of Test Section Mach Number

Figure 4

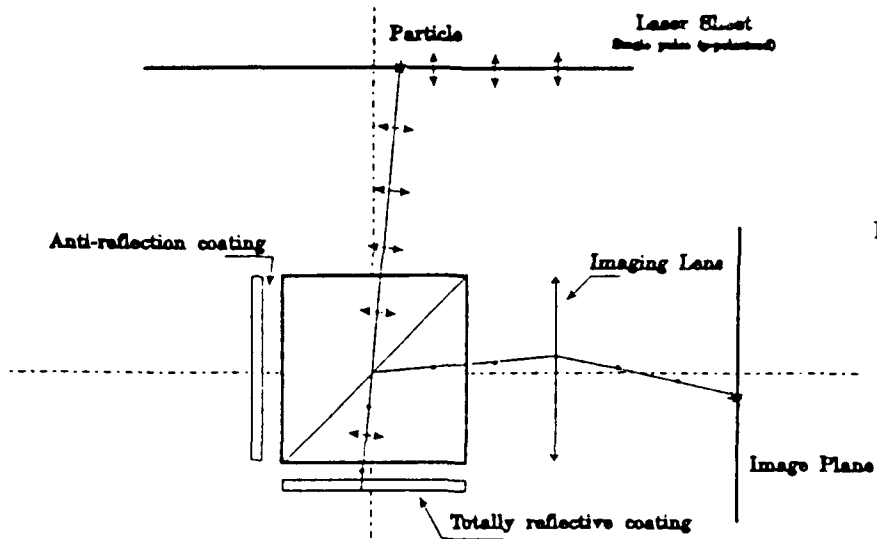


Figure 5(a)

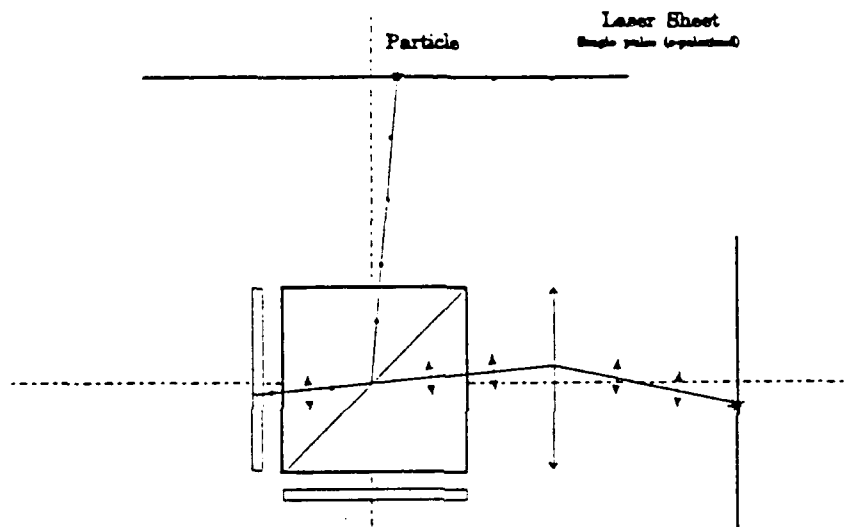


Figure 5(b)

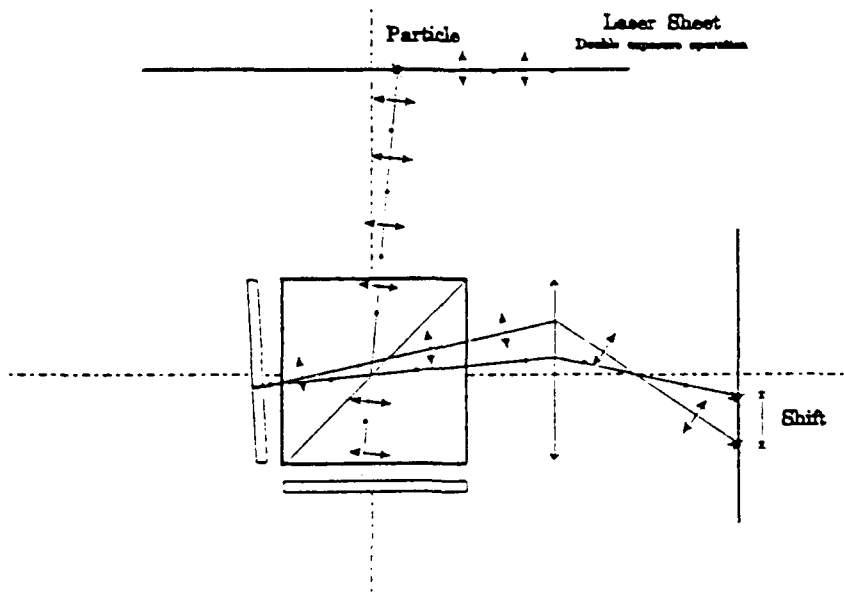


Figure 5(c)

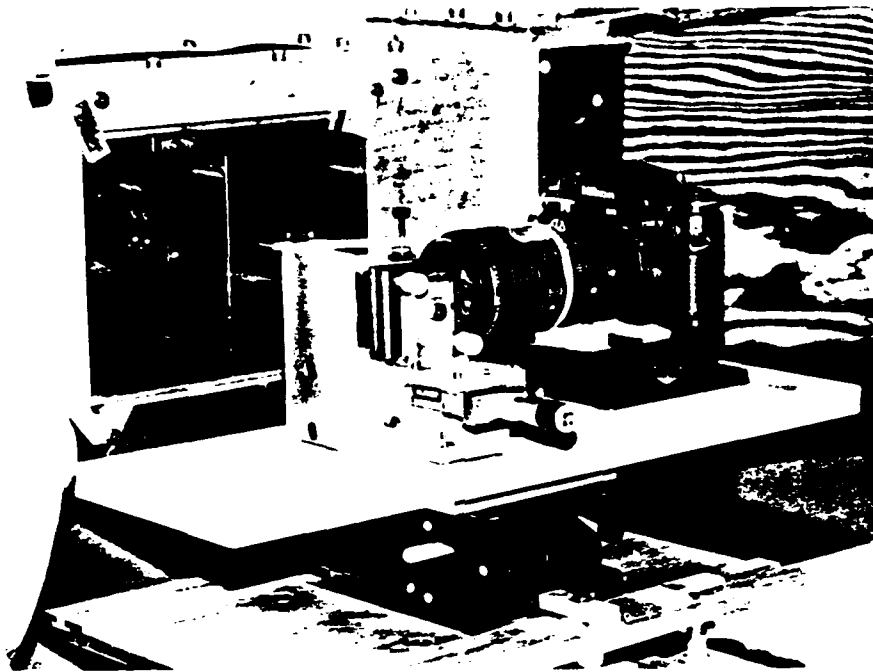
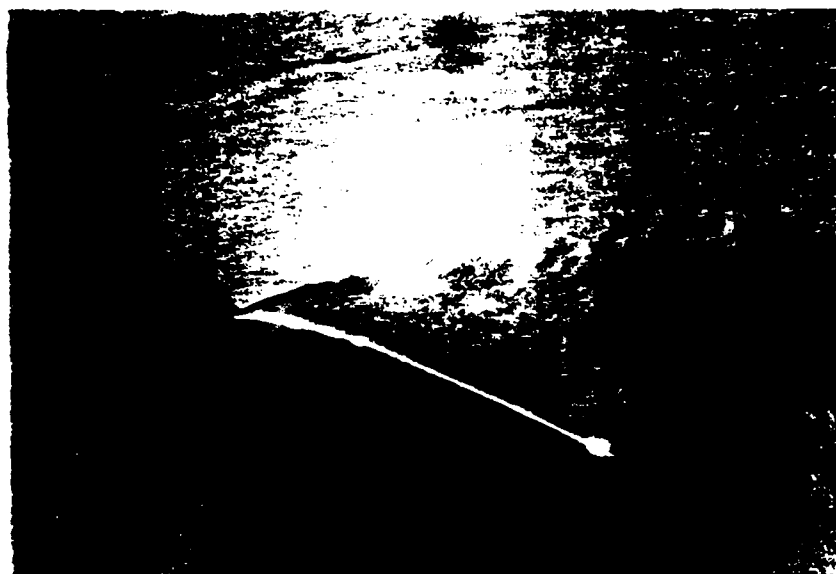


Figure 6



(a)



(b)

Figure 7

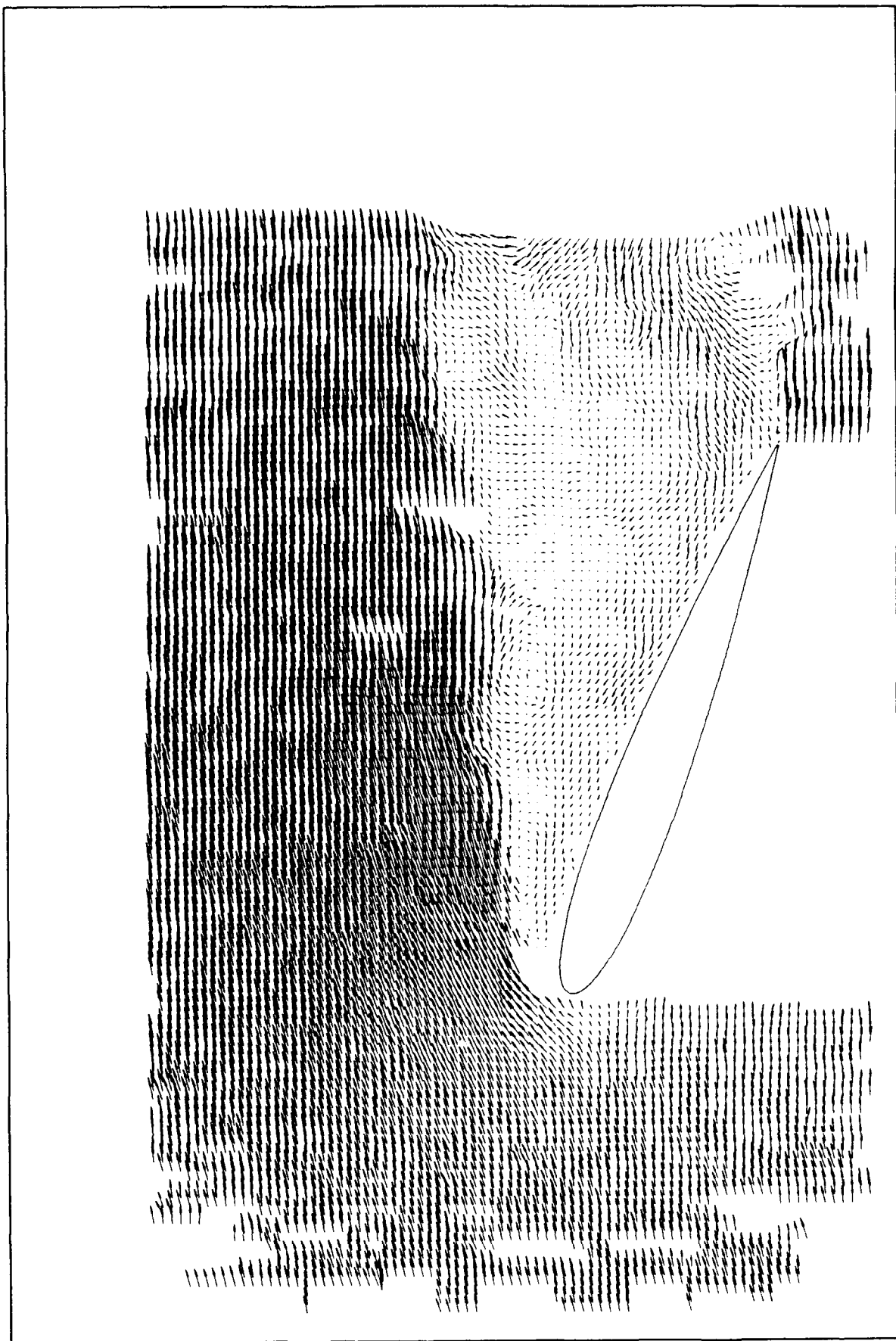


Figure 8 (a)

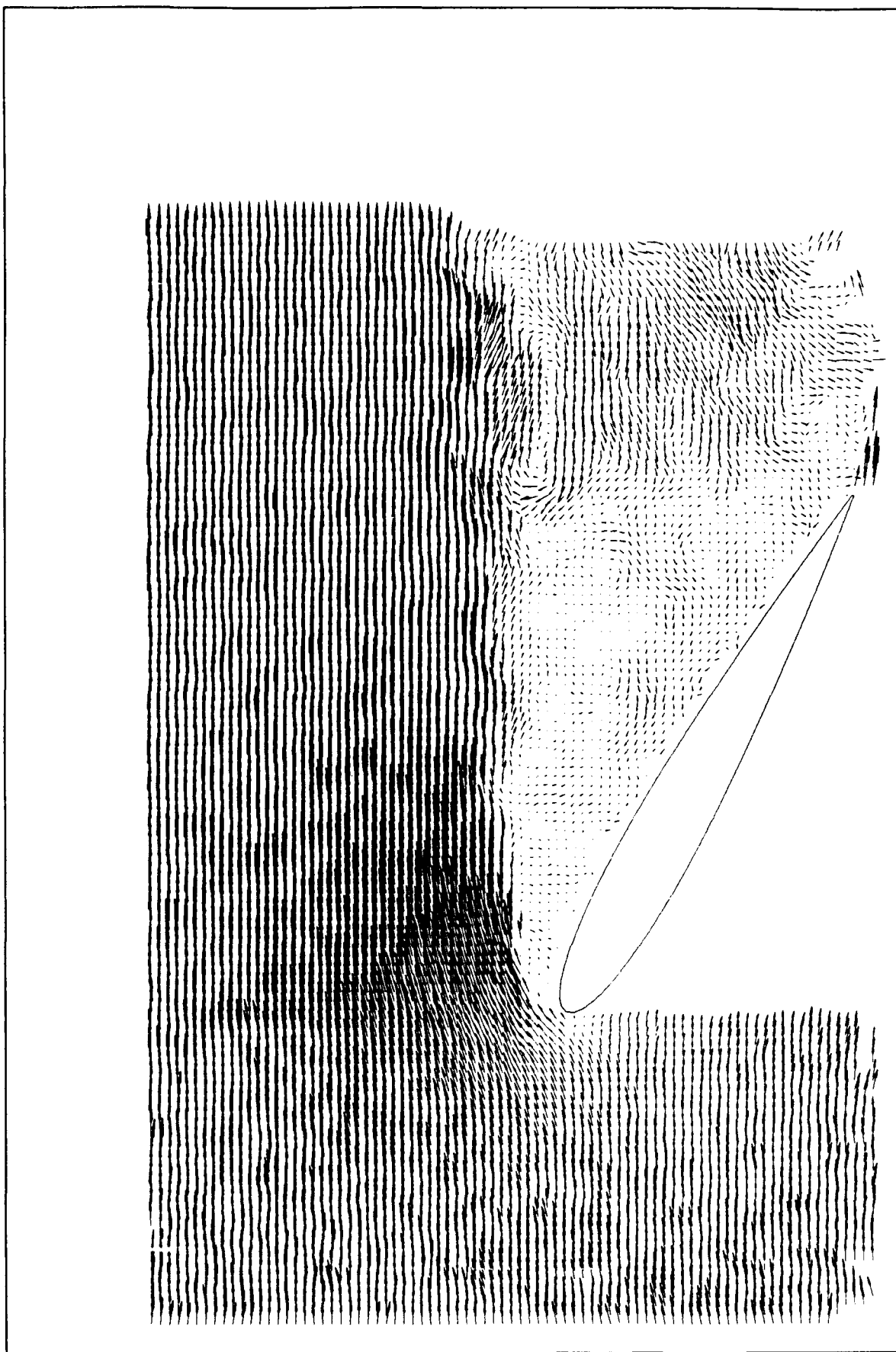
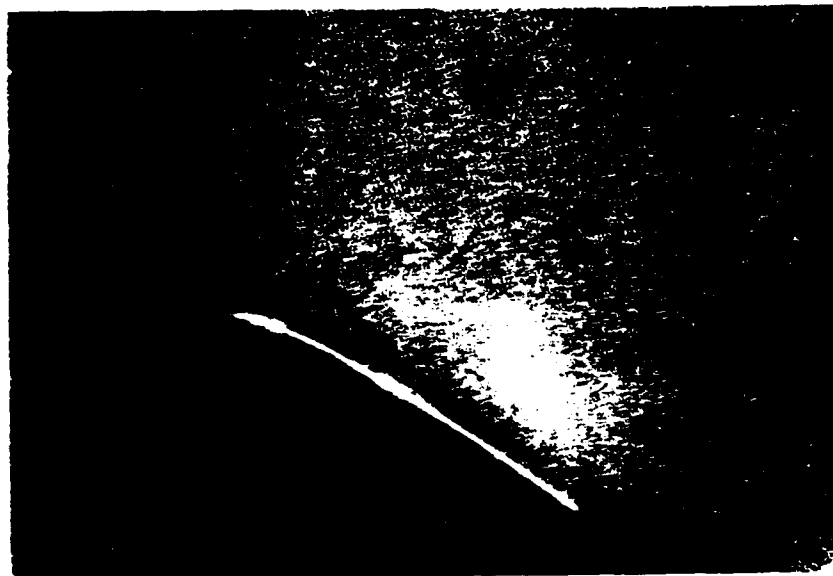


Figure 8 (b)



(a)



(b)

Figure 9

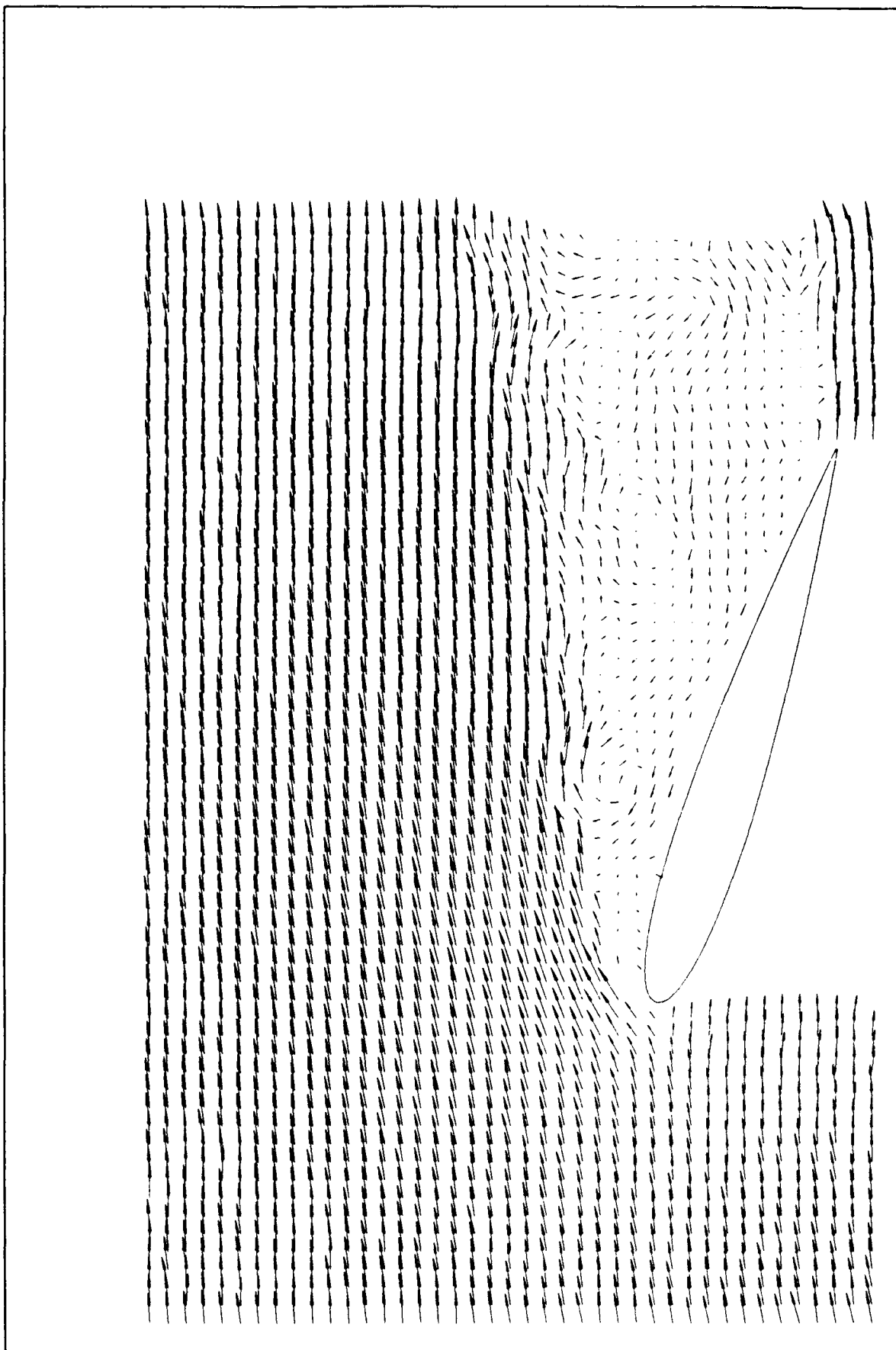


Figure 10 (a)

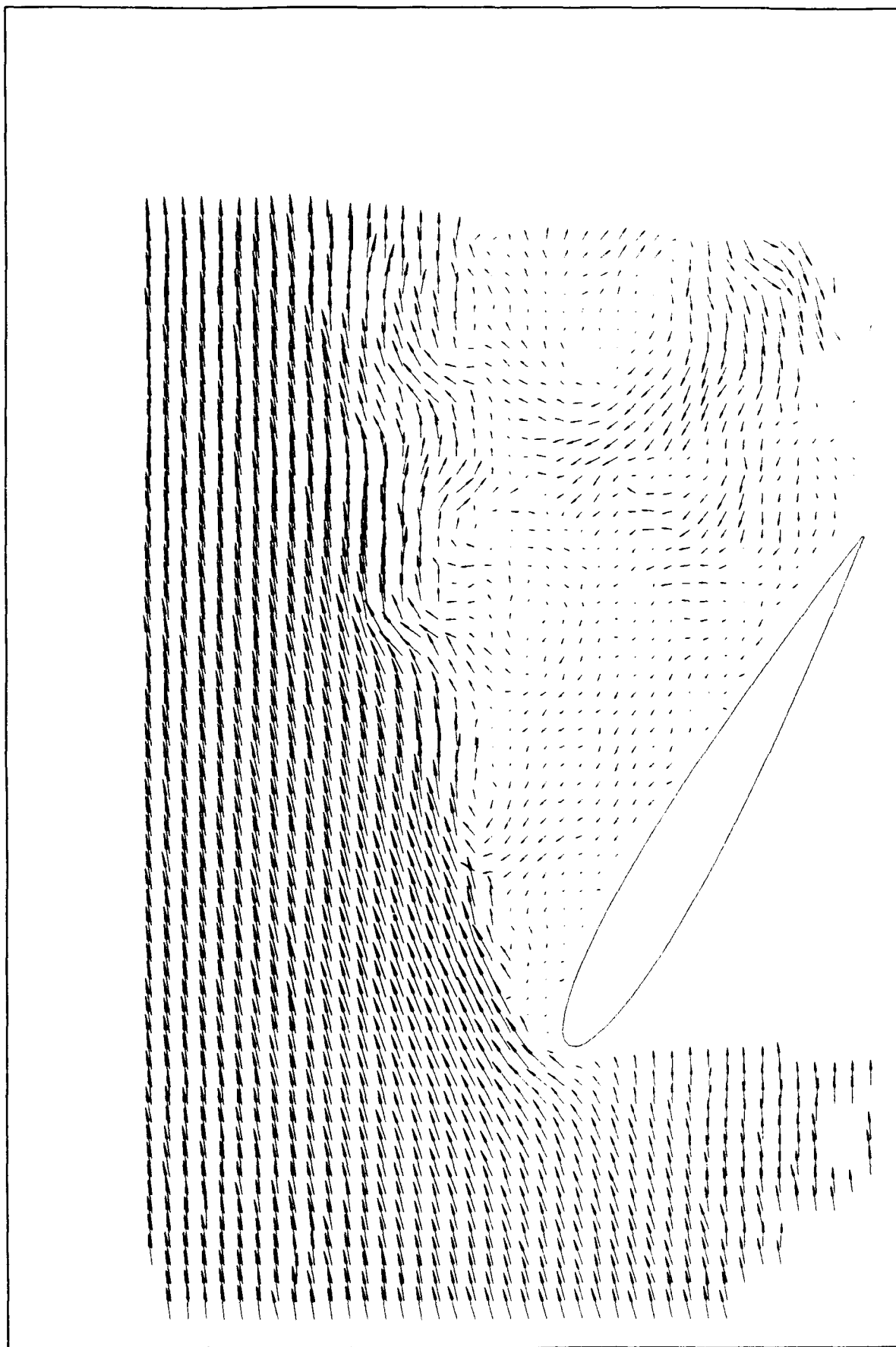


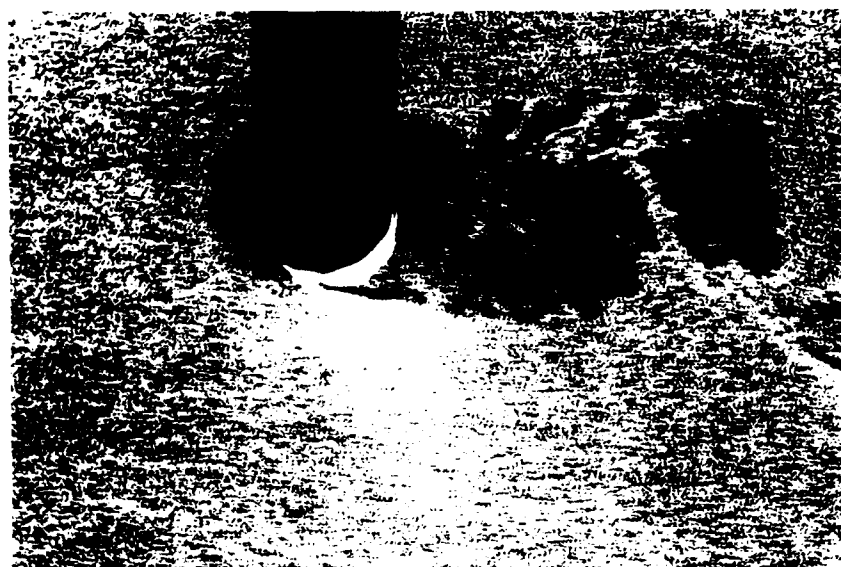
Figure 10 (b)



(a)

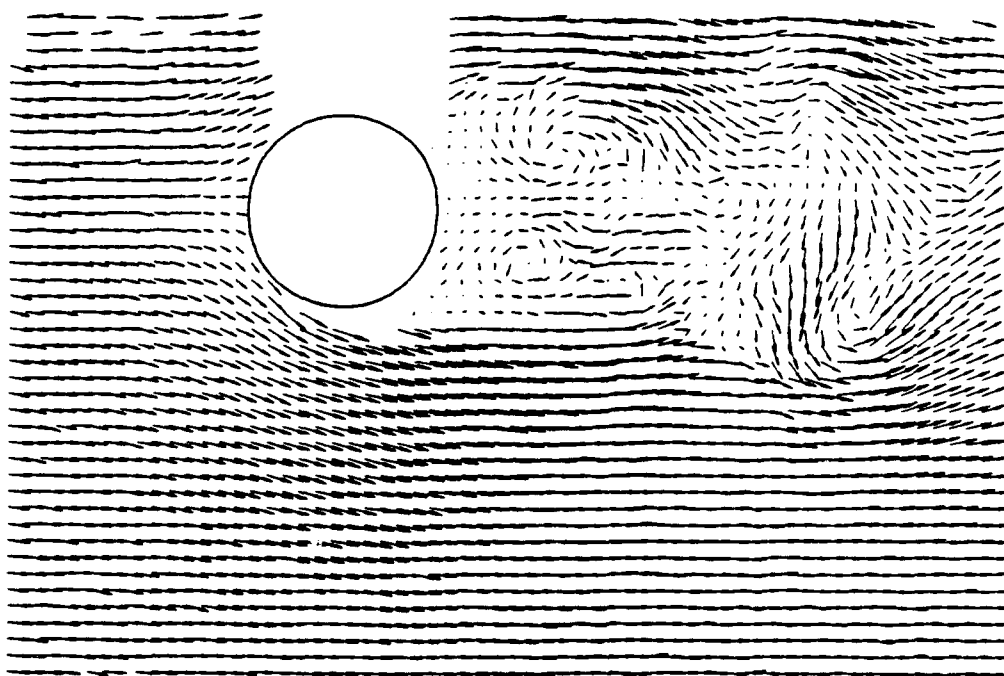


(b)

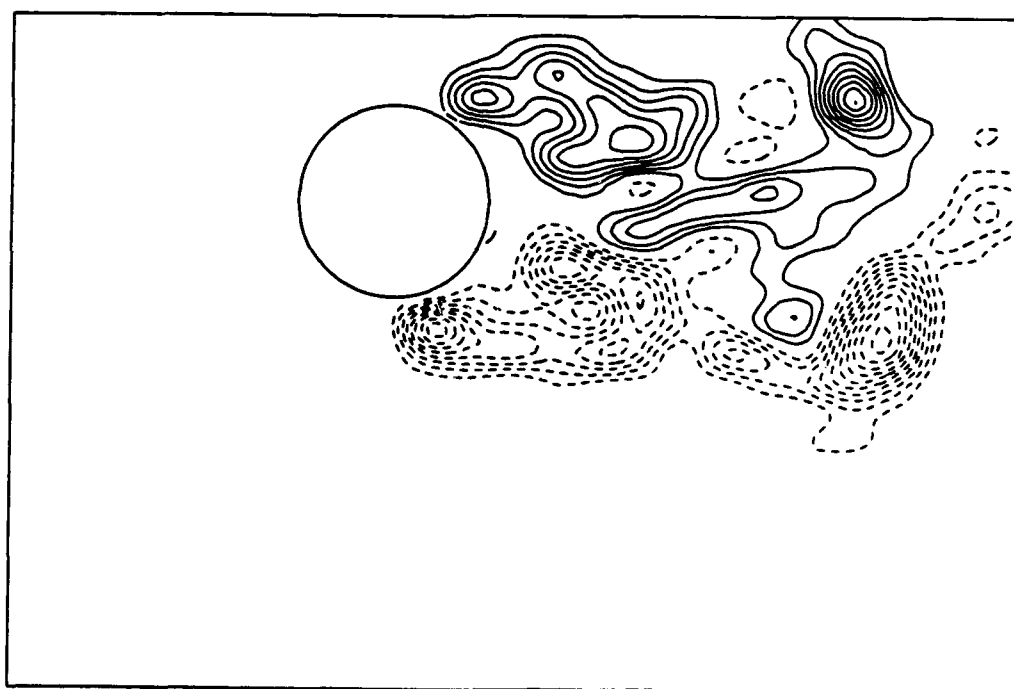


(c)

Figure 11

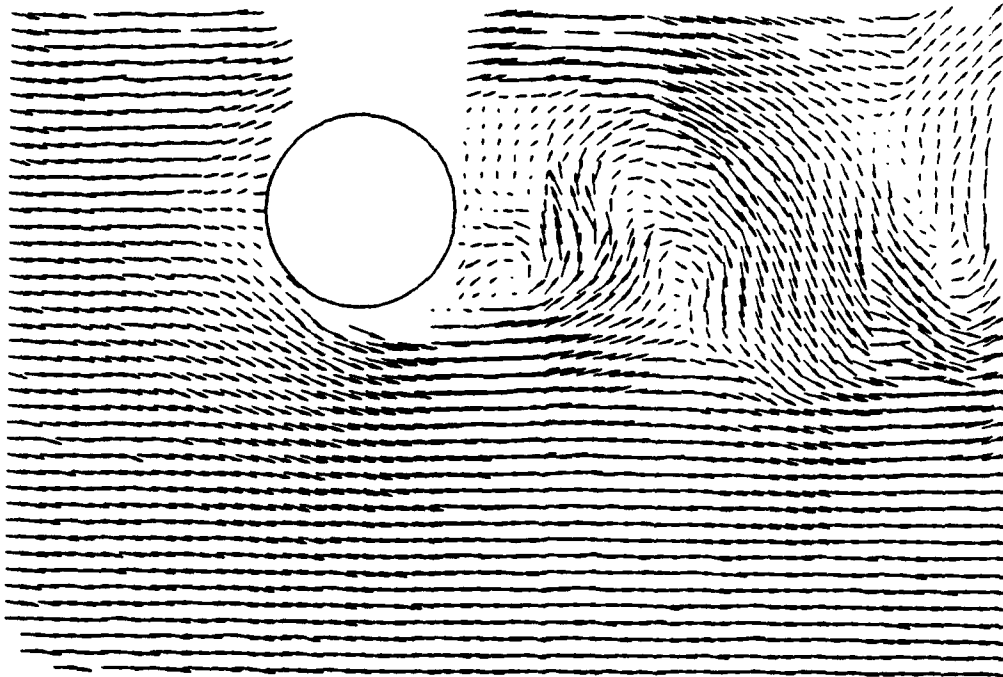


Instantaneous Velocity

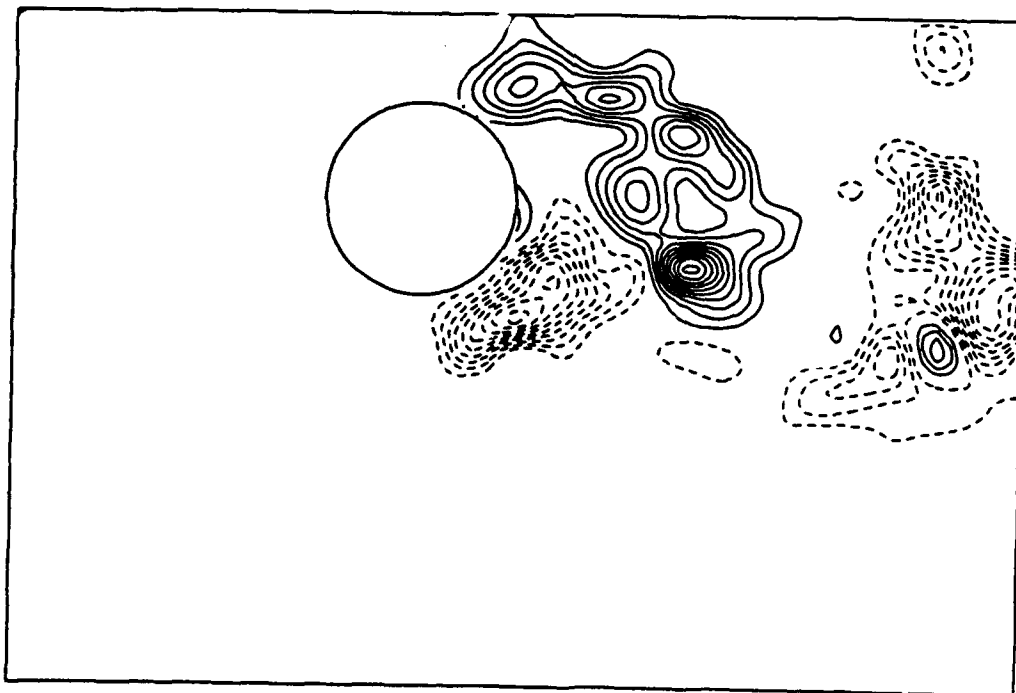


Instantaneous Vorticity

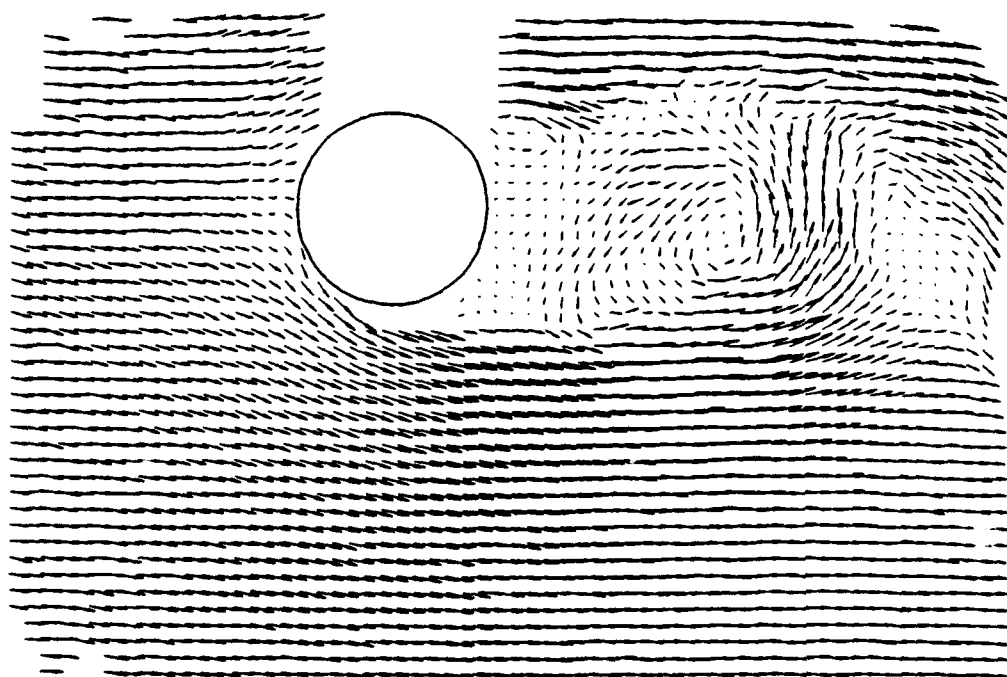
Figure 12 (a)



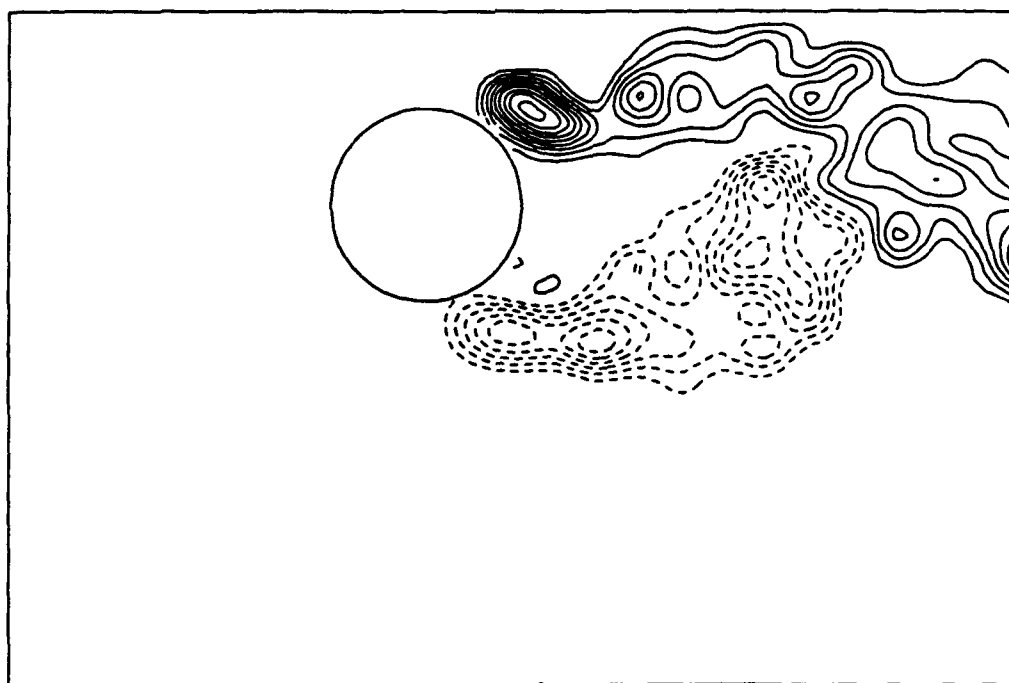
Instantaneous Velocity



Instantaneous Vorticity



Instantaneous Velocity



Instantaneous Vorticity

Figure 12 (c)

APPENDIX A

High Speed Airfoil Flipping Mechanism by Christopher B. Ross

Introduction

A pneumatically actuated high speed mechanism was designed and constructed to "flip" an airfoil through 30° in a subsonic blow-down wind tunnel test section. Previous attempts to get in the 3 msec range through the use of spring actuation were unsuccessful due to the fact that the springs were "mass limited," that is, actuation times would decrease as the spring constants were increased to a point, and then begin to go up due to the mass inertia of the spring itself. This limit was around 4.5 msec.

The problem of mass inertia was overcome by the use of an air piston, in which the force could be increased without any corresponding increase in mass inertia. The only constraint to this method is the material strength limitations of the mechanism itself, some of which were discovered quite by accident.

Experiment Purpose

The purpose of the experiment is to turn impulsively a symmetric NACA 0012 airfoil through 30° from a 0° angle of attack as fast as possible about its $1/4$ chord point. The unsteady stall behind the airfoil will then be studied using a Particle Image Velocimetry (PIV) technique, with interest focused on the aerodynamics of a suddenly pitched airfoil surface in high speed flow (>100 m/s). The PIV data will be correlated with schlieren (optical) experiments of the same airfoil performed independently at another laboratory.

Wind Tunnel Design

The basic design of the facility is shown in Figure 1. High pressure tank air (2000 psi) is reduced through a series of valves to a settling tank stagnation pressure necessary to produce test section velocities in the required 100 to 200 msec range.

The circular settling tank diameter of 17 in. is reduced to the 6x6 in. square test section containing a 1.5 in. chord length airfoil through a smooth converging section. The test section is designed with a window on the top and bottom to allow lengthwise passage of a vertical laser sheet for the PIV technique through the test section (see Figure 2). One side wall contains a 6x8 in. window for camera imaging, where the other side wall is for an aluminum plate and airfoil attachment. The flipping mechanism is attached to the outside of this aluminum plate. The basic airfoil mechanism is shown in Figure 3. A diffusing section exhausts the air to the atmosphere.

Calculations

The most important variable in the calculations of the flipping time for the airfoil is the various masses and rotational moments of inertia of the components of the mechanism. The basic model of the air cylinder pitching mechanism is shown in figure 1. All standard formulas used can be found in basic dynamic systems

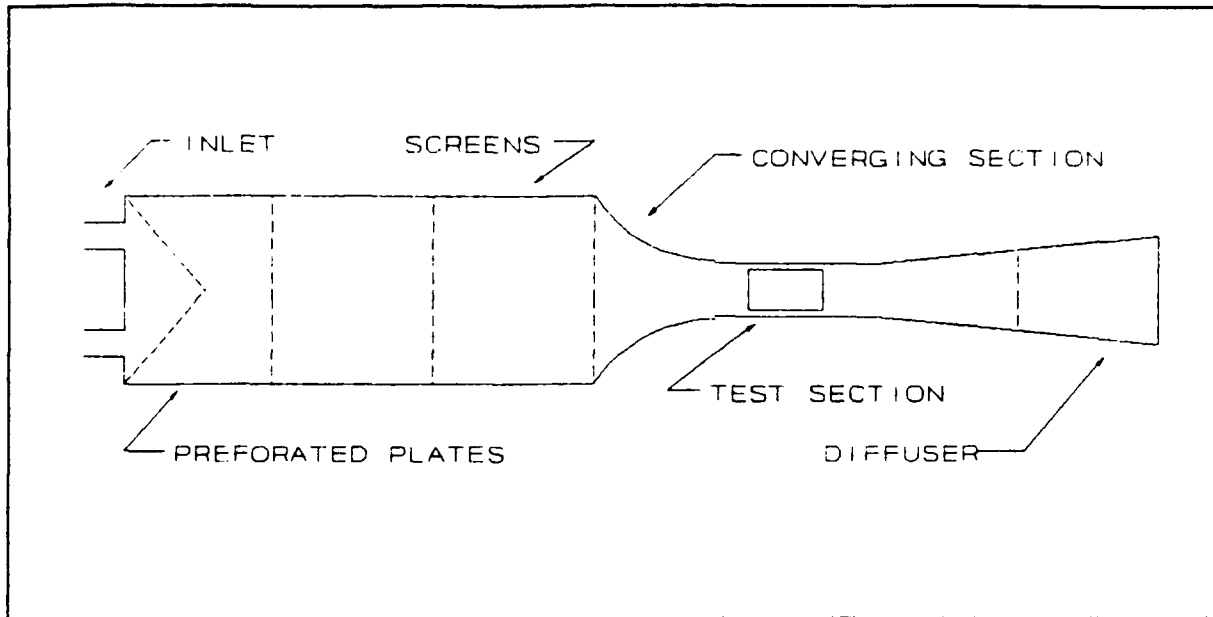


Figure 1: Wind Tunnel Schematic

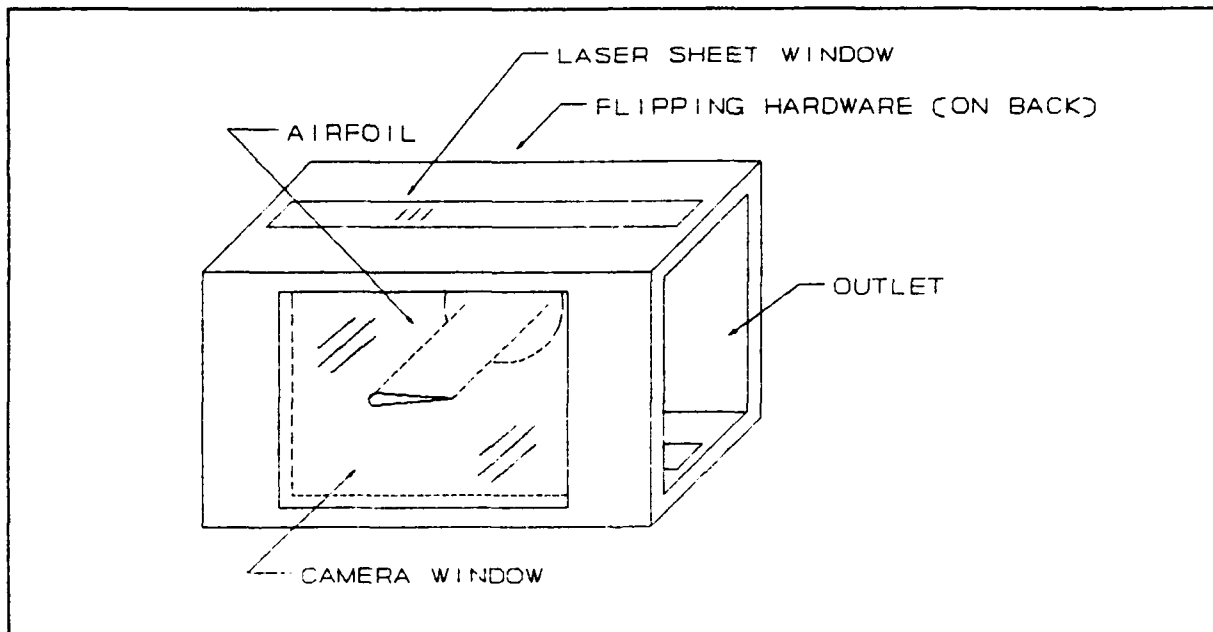


Figure 2: Test Section Detail

textbooks¹.

The rotational moment of inertia of the airfoil is calculated using the integral definition of the moment of inertia about the leading edge and the parallel axis theorem to find the value at the

¹ "Engineering Mechanics: Statics and Dynamics" by R.C. Hibbeler, Macmillan Publishing Company, New York, 1987.

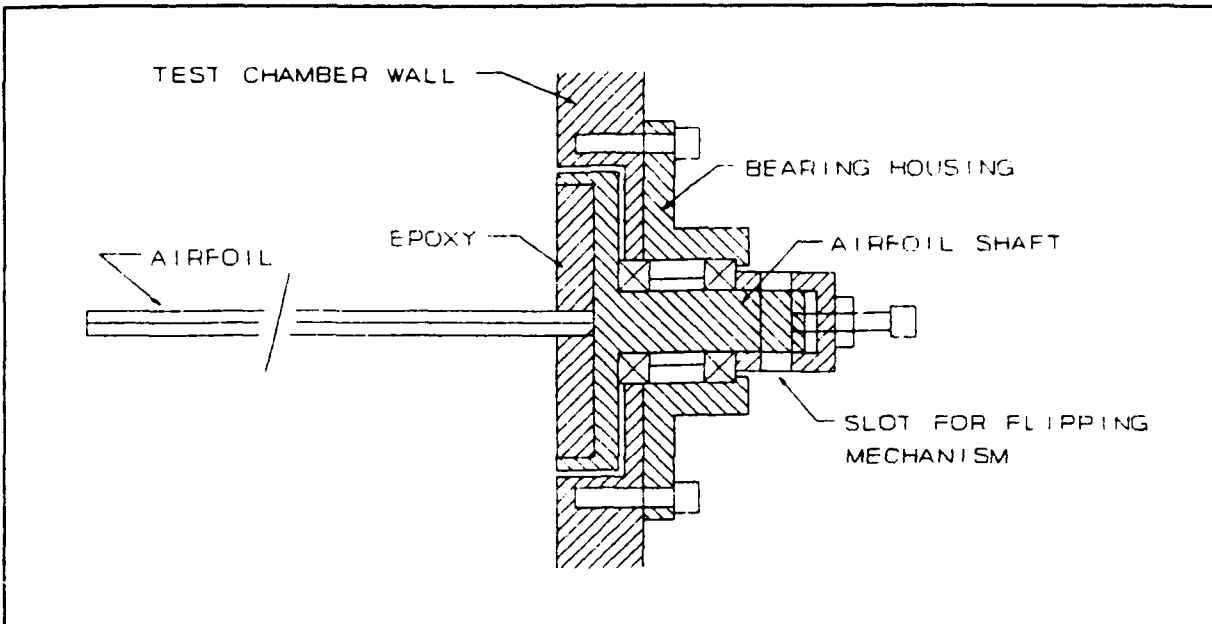


Figure 3: Detail of Airfoil Support Mechanism

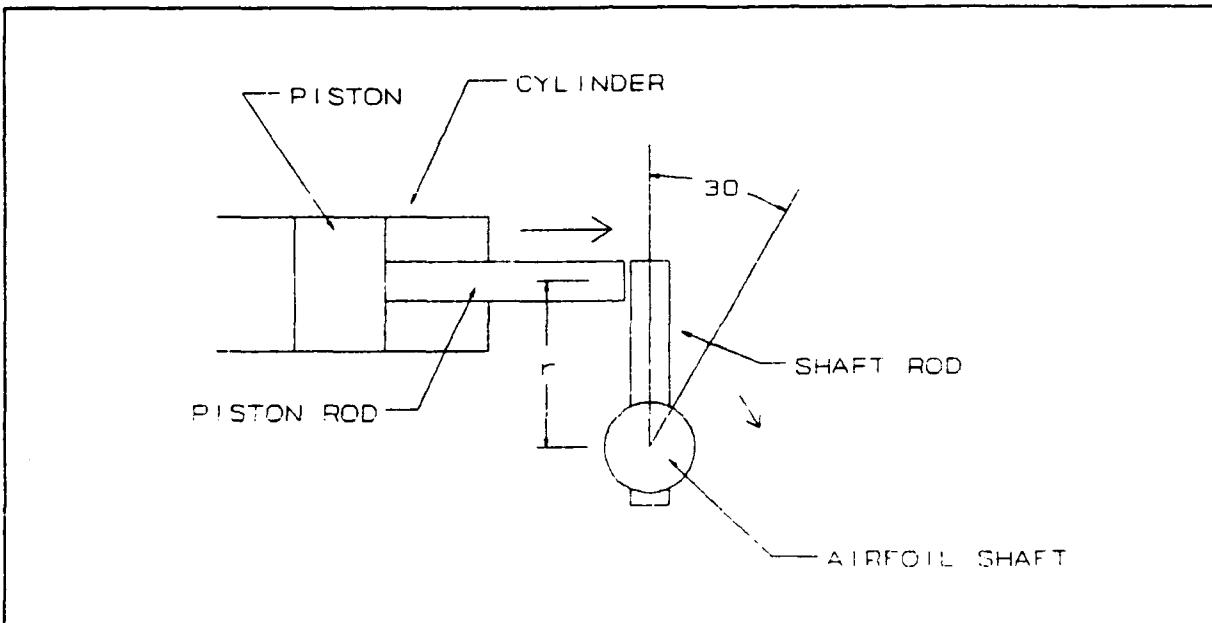


Figure 4: Basic Design of Air Cylinder Pitching Mechanism

1/4 chord point. The differential element was modeled as a thin plate and the corresponding standard formula used. The integral was solved through the panel method by modifying the program that originally produced CNC data points for the manufacture of the airfoil. The original program produced a function $F(x)$ representing the half thickness of the airfoil as a function of the distance x along the chord. Figure 4 shows the panel element and coordinates.

The integral was developed as follows from the basic integral

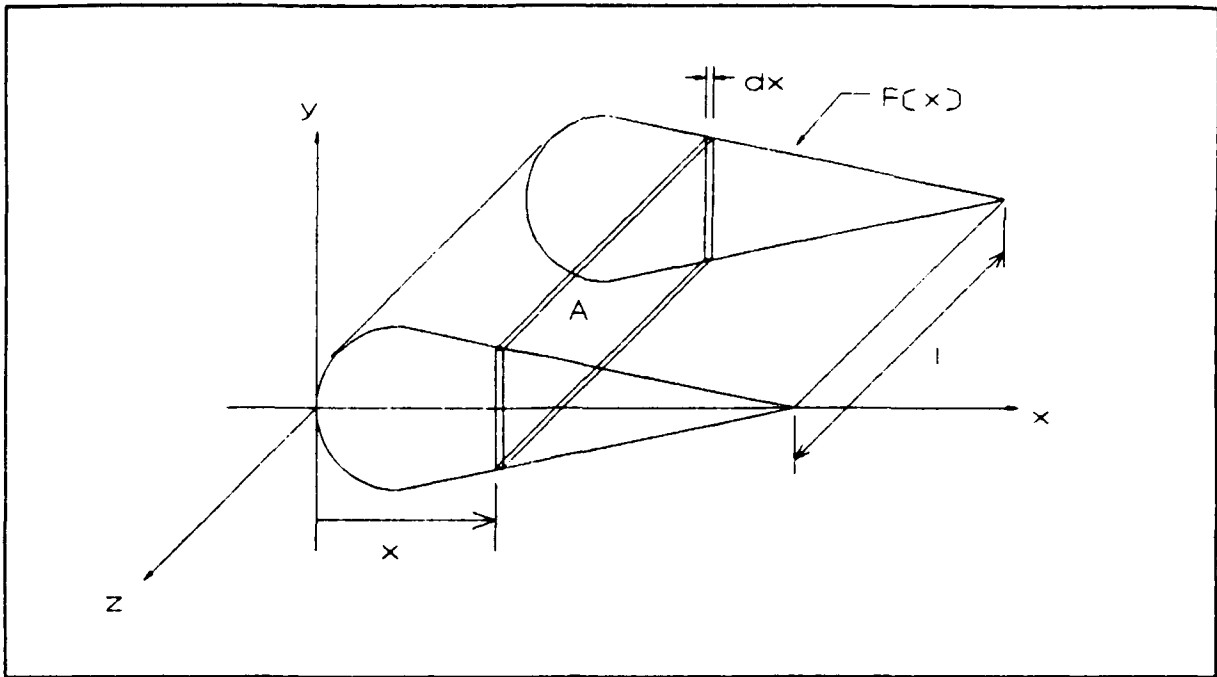


Figure 5: Differential Plate Element for Airfoil

definition of moment of inertia:

$$I_z = \int_0^c dm$$

and from the panel dimensions:

$$dm = \rho dV = \rho A dx = \rho l 2 F(x) dx$$

the differential moment of inertia about the leading edge is:

$$dI_{z'} = \frac{1}{12} [2F(x)]^2 dm$$

by the parallel axis theorem:

$$dI_z = dI_{z'} + x^2 dm = \frac{1}{3} F(x)^2 dm + x^2 dm = \left[\frac{1}{3} F(x)^2 + x^2 \right] dm = \left[\frac{1}{3} F(x)^2 + x^2 \right] \rho l 2 F(x) dx$$

the final integral to be solved:

$$I_z = 2\rho l \int_0^c F(x) \left[\frac{1}{3} F(x)^2 + x^2 \right] dx$$

This gives the moment of inertia about the leading edge, where another application of the parallel axis theorem gives the moment of inertia about the 1/4 chord point.

The program MOM.FOR in Appendix A gave the following values

for the airfoil:

Moment of Inertia About Leading Edge:	$5.30 \times 10^{-5} \text{ kg-m}^2$
Moment of Inertia About 1/4 Chord:	$3.88 \times 10^{-5} \text{ kg-m}^2$
Mass of Airfoil:	0.157 kg

A standard Bimba² double acting air cylinder was found with a piston diameter of 1 1/16 in., piston length of 3/4 in., and a stroke of 12 in. The 5/16 in. shaft was cut to 4 in. and the masses of the aluminum piston and steel shaft were calculated and added to give total piston mass.

mass of piston: 73.9 g

The epoxy and aluminum disk moment of inertia was calculated from standard formulas and original design drawings, as was the shaft moment of inertia.

Disk Inertia:	$4.654 \times 10^{-5} \text{ kg-m}^2$
Shaft Inertia:	$2.85 \times 10^{-7} \text{ kg-m}^2$

The bearing rotational inertia was calculated in a similar manner.

Bearing Inertia: $1.46 \times 10^{-7} \text{ kg-m}^2$

The 3/16 in. lever rod inertia was calculated with a variable radius using standard formulas.

Lever Rod Inertia: $8.713 \times 10^{-7} \text{ r}^3 \text{ kg-m}^2$

The Free Body Diagram for the dynamic system is drawn as shown in Figure 6.

summing moments for the rotational FBD:

$$\sum M=0 \rightarrow -Fr=I\alpha \rightarrow F=\frac{-I\alpha}{r}$$

summing forces for the linear FBD:

$$\sum F=0 \rightarrow F-F_p=ma \Rightarrow F=ma+F_p$$

setting the two above equations equal and solving for the piston force:

² Bimba Air Cylinder: Model 0912-DP, distributed by Adam's Air, Tampa, Florida.

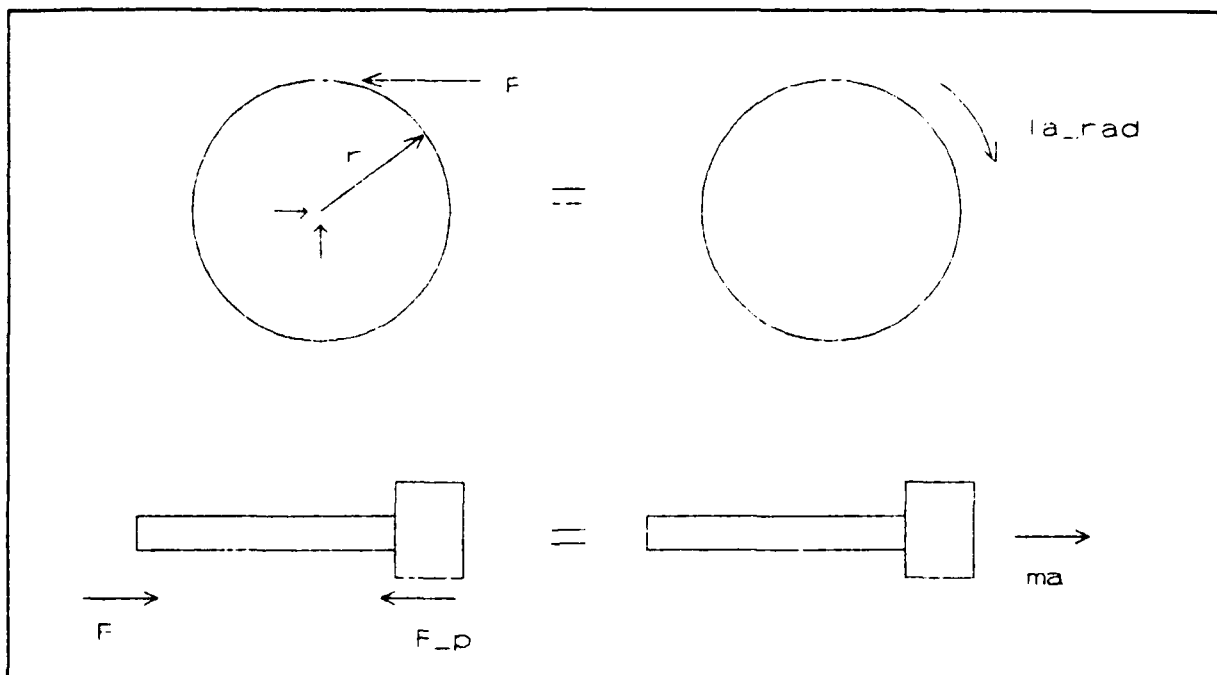


Figure 6: Free Body Diagram for Rotational and Linear Components

$$F_p + ma = -\frac{I\alpha}{r} \text{ with } a_t = \alpha r \rightarrow F_p = -\left(m\alpha r + \frac{I\alpha}{r}\right)$$

solving for the angular acceleration:

$$\alpha = \frac{-F_p}{m_p r + \frac{1}{r}(I_R + I_D + I_S + I_A + I_S)}$$

with the cylinder pressure 130 psi, the angular acceleration as a function of lever rod length r:

$$\alpha = \frac{-512.7r}{7.39 \times 10^{-2} r^2 + 8.713 \times 10^{-7} r^3 + 8.575 \times 10^{-5}}$$

Differentiating this expression with respect to radius r and equating to zero, it is found that the optimum radius is 3.4 cm. This corresponds to an angular acceleration of $1.02 \times 10^5 \text{ rad/s}^2$. Assuming a constant pressure force, hence a constant angular acceleration, the time to travel 30° is found from simple kinematic formulas:

$$\theta = \frac{1}{2} \alpha t^2 = 30^\circ \frac{\pi}{180^\circ} \rightarrow t = \sqrt{\frac{\pi}{3\alpha}}$$

using the above value of angular acceleration, we find:

Theoretical Actuation Time: 3.2 msec

Mechanism design

The requirement of very fast actuation times necessitated an unconventional approach to the use of the air cylinder. Air cylinders usually are filled with air as a movement is required, but the filling process itself takes a relatively long time. The final design uses a pressurized 12 in. throw air cylinder constrained one inch short of full extension by a cam release. When the cam release lever is turned, the piston shaft is released and translates 0.75 in. No air flows through fittings or valves, so actuation time is reduced by an approximate factor of four.

The piston is constrained by the cam release via the lever shaft (see Figure 7) which passes through a slot milled into the thicker piston rod. When the piston has traveled 0.75 in., the piston contacts the cylinder wall, stopping the airfoil from turning past the 30° position. The sudden deceleration of the airfoil and other rotational components was initially violent enough to shear the lever shaft, but successive heat treatments of components alleviated the problem.

Experimental Results

A set of optical sensors was attached to the mechanism to signal approximate starting and stopping positions of the airfoil. The time between signals, or the actuation time, was recorded using a pulse counter. The actuation time vs. cylinder pressure was recorded and plotted for a calibration curve to observe consistency (Figure 8). The smooth curve obtained suggests that the actuation device is very repeatable, and that a specified time may be obtained by properly varying the cylinder pressure.

The apparent better-than-theory results obtained may be explained by the fact that the airfoil has to move a finite distance to trigger the optical sensor that begins the timing action, so the time of the first 2° of motion is not accounted for. The airfoil is moving relatively slowly at this initial point and a considerable error of around 20% is incurred in the calibration chart, thus showing a lower actuation time than is actually occurring. The error in the second optical sensor is of no consequence, as the airfoil is traveling at a very high angular velocity during the final 2°.

Conclusions

The advantage of the air-actuated flipping mechanism for the impulsively stalled airfoil experiment has been demonstrated. The system is not mass limited as is the case of a spring-actuated flipping mechanism. The time may be reduced by increasing the cylinder pressure exponentially, as demonstrated by Figure 8.

True calibration curved may be produced by the addition of an optical shaft encoder to the present system. This would allow precise (1/10 degree) measurement of the angular position of the airfoil and successive differentiations would give accurate angular

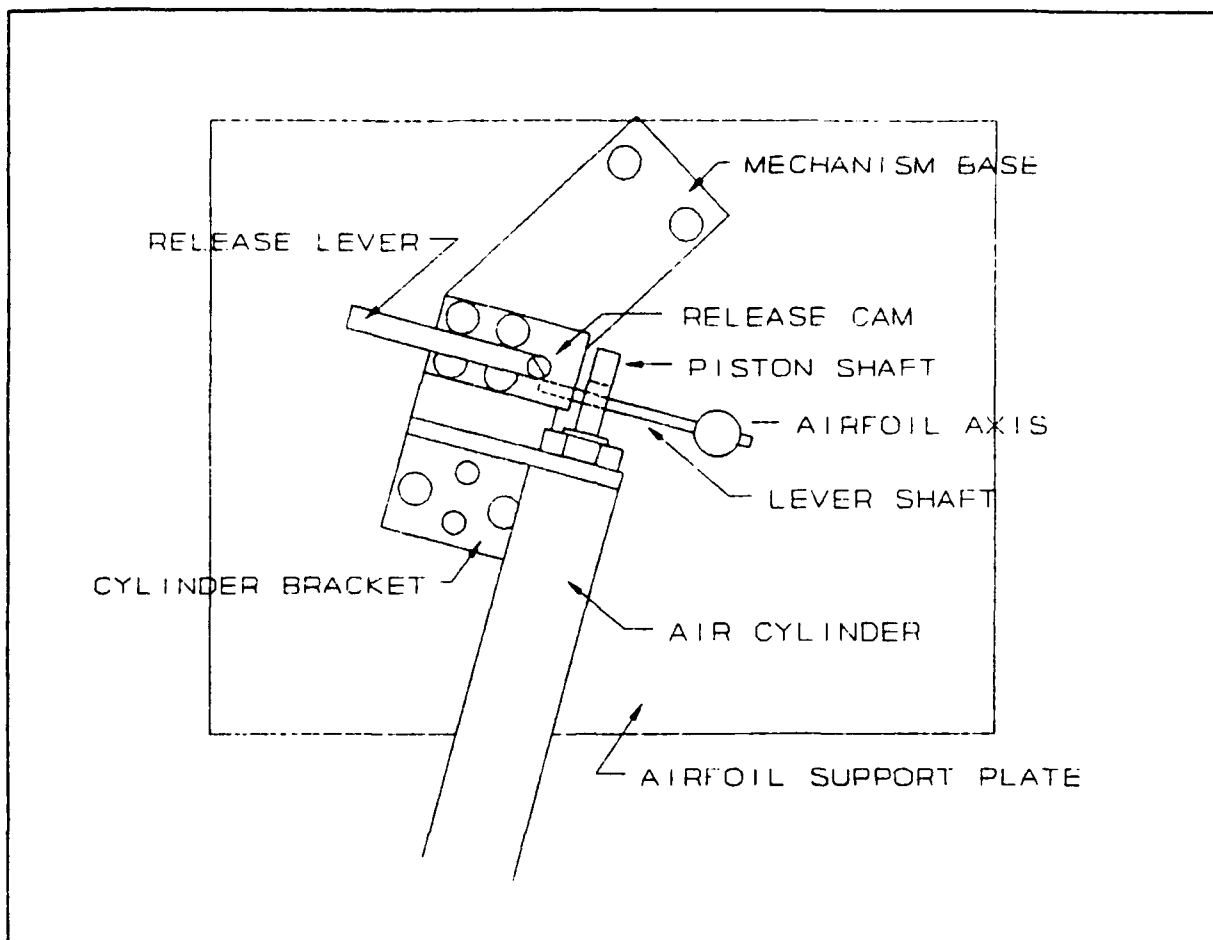


Figure 7: Scale Schematic of Airfoil Actuating Mechanism

velocities and accelerations.

The calculations and basic procedures of this project may be applied to any rotational/translational system where considerable masses must be accelerated at very high rates. All calculations also may be done on a modern scientific calculator.

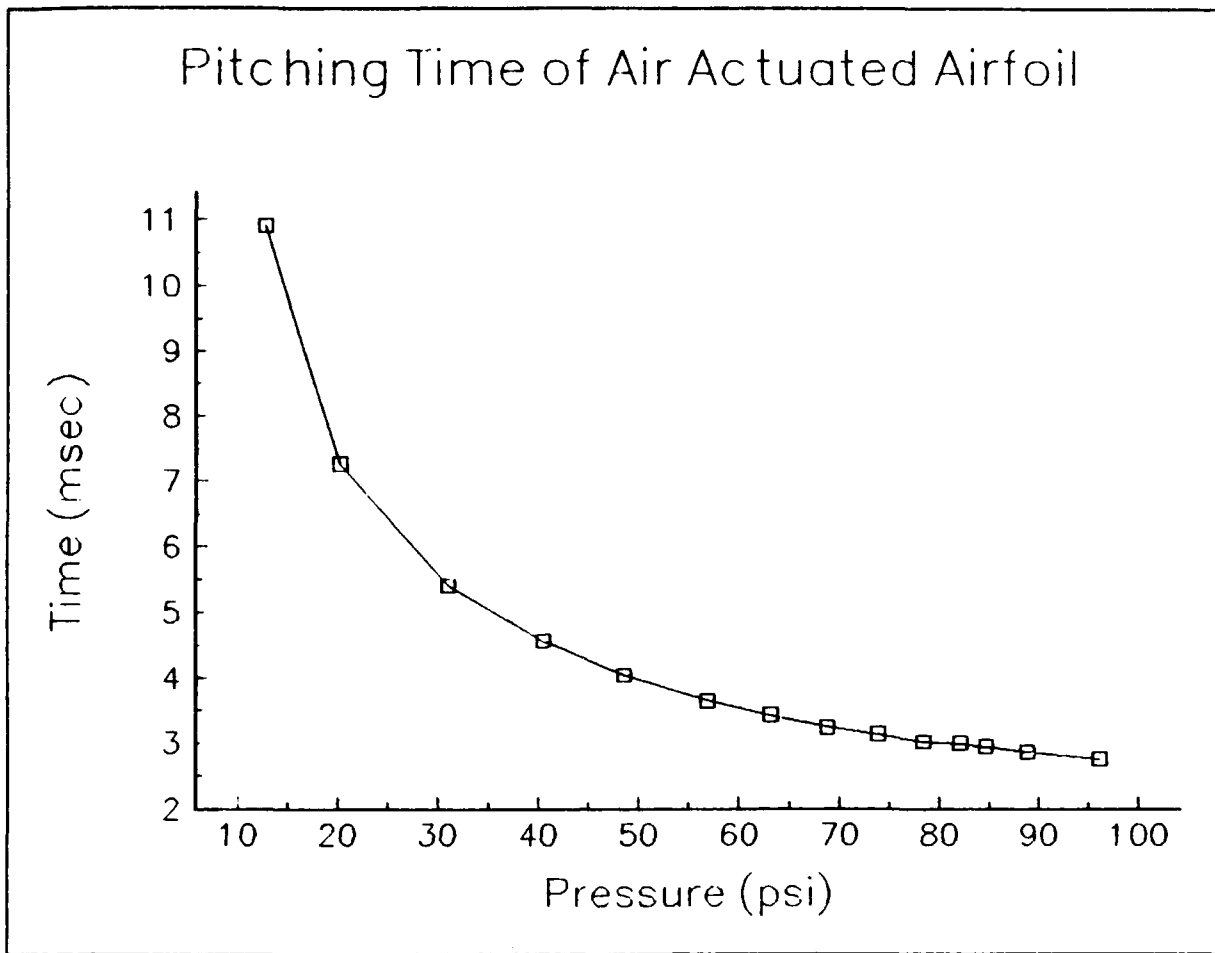


Figure 8: Pitching Calibration Time

APPENDIX A

```
program mom
c
integer jmax
real thick, chord, c, c1, c2, c3, c4, c5, step, m, IC4
  REAL I,RHO,L,X1,Y1
c
parameter (jmax= 201, thick= 0.12, chord= 1.5)
dimension x(jmax), y(jmax)
c
c= thick/0.05
c1= 0.2969
c2= -0.126
c3= -0.3516
c4= 0.2843
c5= -0.1015
step= 1.0/float(jmax - 1)

  RHO=8440.0
  L=6.16*0.0254
  I=0.0
  m=0.0
c
do 10 j= 1,jmax
  x(j)= float(j-1)*step
  xpos= x(j)
  y(j)= c1*sqrt(xpos) + xpos*(c2 + xpos*(c3 + xpos*(c4 +
:      xpos*c5)))
  x(j)= chord*x(j)
  y(j)= chord*y(j)*c/4.0
  X1=X(J)*0.0254
  Y1=Y(J)*0.0254
  I=I+Y1*(1.0/3.0*Y1**2+X1**2)*CHORD/JMAX*0.0254
  m=m+y1*CHORD/JMAX*0.0254
  write (2,15)( x(j),',',y(j))
10 continue
  I=I*2.0*RHO*L
  m=m*2.0*rho*L
  IC4=I-M*(0.25*CHORD*0.0254)**2
  PRINT*, 'MASS MOMENT OF INERTIA (LEADING EDGE): ',I,'
+ KG-M^2'
  PRINT*, 'MASS MOMENT OF INERTIA (C/4 POINT): ',IC4,'
+ KG-M^2'
  print*, 'MASS: ',M,' KG'
15 format(f8.5,a3,f8.5)
end
```

APPENDIX B

A Hybrid Grid Approach to Study Dynamic Stall

Taekyu Reu* and Susan X. Ying†

*Supercomputer Computations Research Institute
Mechanical Engineering Department FAMU/FSU
The Florida State University
Tallahassee, FL 32306*

A hybrid structured and unstructured grid scheme is developed to study dynamic stall over an airfoil in a wind tunnel. The unsteady Navier-Stokes equations are solved implicitly using this hybrid grid scheme. Results are compared with experimental data. Additionally, they reveal informative details of the flow field physics associated with dynamic stall.

Introduction

The objective of this work is to develop an efficient hybrid-grid algorithm to study the dynamic stall over a pitching airfoil. In particular, this numerical simulation will be used to predict the physics including wind-tunnel wall interference.

The dynamic stall over a pitching airfoil is characterized by unsteady flow separation and the formation of a leading edge vortex. Development of these unsteady phenomena produces significant differences in the aerodynamic performances compared to steady flows. Understanding dynamic stall is important for designing aircraft, rotor blades and wind turbines. The control and utilization of the aerodynamic loads induced by these physical phenomena requires insight into the unsteady flow field.

At the Florida State University, the particle image displacement velocimetry (PIDV) technique¹ has been developed to measure the unsteady flow field velocity vectors. The complexity and rapidity of the flow development makes this experiment very challenging and difficult. Furthermore, the experimental study of dynamic stall over an airfoil is complicated by the wind-tunnel wall interference. The measurements must be corrected on the basis of steady calibrations. While the PIDV data is not yet available, our numerical solutions will be

* Research Scientist, currently at BAe, North Humberside, U.K., AIAA Member

† Assistant Professor, SCRI-line faculty, Member AIAA

used to predict the wall interference and compared to the PIDV measurements. Numerical flow visualization will also be used to study flowfield details of dynamic stall. The AGARD data², already corrected by calibrations, is used to verify the computed results in this work.

Numerical simulation of a pitching airfoil in a wind tunnel presents several challenges. The first and the most important one is to capture the unsteady flow separation phenomenon. This requires accurately resolving the unsteady boundary layer development around the airfoil. The second challenge is simulating the formation and evolution of the vortical structures on the leeward side of the airfoil. The third challenge, also identified by a number of researchers,³⁻⁵ is the effect of compressibility in dynamic stall. In particular, the effects of the shock wave formation on the leading-edge vortex. This issue will not be addressed in this work, rather a Mach 0.3 flow is investigated. Lastly, moving and confining the airfoil between the wind tunnel walls requires a delicate numerical approach. That is, one needs to re-grid or interpolate at each time step. Consequently, in addition to solving the unsteady flow equations, a considerable amount of CPU time will be used for interpolation or to compute the transient grids. These physical and numerical challenges necessitate formulation of an efficient Navier-Stokes algorithm that integrates the unsteady grid strategies to the flow solution procedure.

In this research, the approach is to couple structured grids and unstructured grids. The motivation in this hybrid grid scheme is to explore ways which can efficiently and accurately simulate the complex physical phenomena due to dynamic stall. However, this method is not limited to simulating dynamic stall. This hybrid grid scheme can be applied to many internal unsteady flow problems, such as the flow around compressor or turbine blades in jet engines. The grid topology for simulating a pitching airfoil in a wind tunnel is not such a complex one. Yet comparing to a general single-grid approach, such as an adaptive remeshing finite element method⁶, this hybrid grid approach will be still less expensive for resolving the unsteady boundary layers. That is, by utilizing a structured, highly stretched, body-conforming grid around the airfoil, the gradients in the wall region can be very efficiently resolved. This is critical in simulating the physics of unsteady viscous flows.

In contrast to the single adaptive unstructured grid approach, there are also multi-zone patched grid methods and overset grid methods. These methods employ multiple structured grids for unsteady Navier-Stokes simulations. It has been demonstrated^{7,8} that these methods can simulate the unsteady motion where one component moves with respect to the others. Nevertheless, the interpolation procedure for these methods is not vectorizable.

Consequently the computation time required for interpolation can be comparable to that of the flow solver at each time step, especially for the overset grid case. The approach for this work is similar to the multi-zone patched grid method. The major difference is in the application of unstructured grids. At each time step, an unstructured grid is used to patch the structured grids, thereby avoiding the excessive time necessary for interpolation. This approach will be referred to as the dynamic structured and unstructured grid (DSUG) method. The trade-off here is in the grid generation at each time step. Again, it should be noted that even though for this particular problem, the geometries do not necessitate the use of an unstructured grid, the DSUG method can be readily generalized for more complex unsteady problems, and this work is only a start.

While the DSUG approach can be very general and robust, for modelling the flow over a pitching airfoil in wind tunnel, one can employ a simpler but less general method. This method uses “rigid” patched grids, allowing the inner grid to rotate while the outer grid stays fixed. As a result there is a circular “slip boundary” in the domain and flow variables are interpolated across this boundary. This approach has been investigated by Rai,⁹ and the DSUG approach will be compared to it. However, in this work the slip boundary is embedded in the unstructured grid domain, different from that of Ref. 9. This procedure will be referred to as the patched structured and unstructured grid approach (PSUG). Figures 1a and 1b show a comparison of snap shots (at $\alpha = 3.82^\circ$) of grids around the airfoil for these two approaches. In the next section, the numerical method will be described. Then the DSUG and PSUG approaches will be compared in terms of coding complexity and computational effort for an inviscid simulation. Finally, the results of dynamic stall at a reduced frequency of 0.02546, flow Mach number 0.3, and Reynolds number 2.7×10^6 are presented.

Numerical Method

The two-dimensional Navier-Stokes equations in non-dimensionalized integral form are solved. These equations in Cartesian coordinates are given by

$$\frac{\partial}{\partial t} \iint_{\Omega} Q dA + \oint_{\partial\Omega} (F dy - G dx) = 0, \quad (1)$$

where Q is the conservative variables vector consisting of density, x and y momentums, and total energy per unit mass. The flux vectors F and G include both inviscid and viscous terms.

Spatial Discretization

An upwind cell-centered finite volume method is used to evaluate the flux integral in eqn. (1). For an arbitrary k th cell with edges e_j , equation (1) can be written in a semi-discretized form as

$$\left(\frac{\partial \hat{Q}V}{\partial t}\right)_k + \sum_{j=1}^n (F\Delta y - G\Delta x)_{e_j} = 0, \quad (2)$$

where \hat{Q} is the cell averaged value of the conservative variables vector and V is the area of the k th cell such that $\hat{Q}V = \int_V Q dV$. The summation of the fluxes in equation (2) is over the cell faces (or "edges",) where n is 3 for a triangular cell and 4 for a rectangular cell.

For computing the inviscid flux terms on the structured grid, primitive cell-center variables, \hat{Q}_p (includes density, x and y components of velocity and pressure), are extrapolated to the cell interface (edge) by using an upwind-biased interpolation.¹⁰ Roe's flux-difference scheme¹¹ is used for flux formulation. Similar approach is applied to compute the flux terms on the unstructured grid. As illustrated in Fig. 2. variables at the edge e_3 inside the k th triangle (\hat{Q}_{pi}) are obtained using \hat{Q}_K , \hat{Q}_{III} , and \hat{Q}_3 . Similarly, variables at the edge e_3 just outside the k th triangle (\hat{Q}_{po}) are obtained using \hat{Q}_K , \hat{Q}_{III} , and \hat{Q}_n . The vertex variables such as \hat{Q}_1 and \hat{Q}_n are obtained by averaging cell values around vertices. Since the viscous phenomenon in dynamic stall originates from the airfoil surface, and it is most dominant near the airfoil, viscous terms are evaluated only in the C grid around the airfoil. This inviscid/viscous approach can be found in Ref.12 for steady state cases. Second order central differencing is used for all viscous terms, and the Baldwin-Lomax eddy viscosity model¹³ is employed for turbulent flow simulations.

Temporal Discretization

The semi-discrete governing equation (2) can be written in an operator form as

$$L(\hat{Q}) = \frac{\partial(\hat{Q}V)}{\partial t} + R(\hat{Q}) = 0. \quad (3)$$

Applying the Euler implicit method to this equation yields

$$L(\hat{Q}^{n+1}) = R(\hat{Q}^{n+1}) + \frac{I}{\Delta t} \left[\left(1 + \frac{\phi}{2}\right)(\hat{Q}V)^{n+1} - (1 + \phi)(\hat{Q}V)^n + \frac{\phi}{2}(\hat{Q}V)^{n-1} \right]. \quad (4)$$

This equation is first order time accurate when $\phi = 0$, and second order time accurate when $\phi = 1$. It can be solved iteratively by using the Newton's method. Rearranged in Delta form, equation (4) becomes

$$\left[\left(1 + \frac{\phi}{2}\right) \frac{V^{n+1}}{\Delta t} - \frac{\partial R(\hat{Q}^l)}{\partial \hat{Q}} \right] \Delta \hat{Q}^l = -R(\hat{Q}) - \frac{I}{\Delta t} \left[\left(1 + \frac{\phi}{2}\right) \hat{Q}^l V^{n+1} - (1 + \phi)(\hat{Q}V)^n + \frac{\phi}{2}(\hat{Q}V)^{n-1} \right], \quad (5)$$

where l is the sub-iteration index in each time step. The unknown vector $\Delta\hat{Q}^l$ is defined as $\Delta\hat{Q}^l = \hat{Q}^{l+1} - \hat{Q}^l$. At convergence of each time step, $\Delta\hat{Q}^l = 0$, and $\hat{Q}^l = \hat{Q}^{n+1}$. Local time steps are used to accelerate the convergence rate for the sub-iterations.

To further accelerate the solution procedure, left hand side of eqn. (5) is factored using the approximate factorization method¹⁴ for the structured grid. For the unstructured grid, vectorization is achieved by utilizing a multi-coloring method¹⁵.

Domain Decomposition

The physical space is split into several sub-domains each having a simple grid topology (see Fig. 3). Body conforming structured grids are generated to enclose the wall regions including the airfoil surface (sub-domains II, III, and VI in Fig. 3). Each of these grids is generated independently and a gap is left between sub-domain boundaries. An elliptic grid generator¹⁶ was used for the C grid surrounding the airfoil. Sub-domains I and VII are filled by simple Cartesian grids. It is trivial to generate these Cartesian grids and they do not require metrics computation in solving the conservation laws. The gap between the body-conforming grid and the Cartesian grids is filled with an unstructured grid. The unstructured grid is generated using the Delaunay triangulation.¹⁷ This grid is initially generated from boundary node points and new node points are added at the center of the triangles which have larger cell area than the expected value. This is repeated until an acceptable unstructured grid is obtained and Laplacian smoothing¹⁸ is used at each iteration.

Since the C grid and the inner unstructured grid rotate as a rigid body in the PSUG approach, remeshing is not required at each time step. However, in the DSUG case, the unstructured grid must be generated at each time step as the airfoil and the C grid rotate. To compute the grid at each time step, locations of new node points are obtained by modeling cell edges as springs with the spring stiffness inversely proportional to the edge length¹⁹.

Boundary Conditions

Characteristic boundary conditions based on Riemann invariants are used for inflow and outflow boundaries. Tangential boundary conditions are applied for the wind tunnel walls. On the airfoil surface no slip boundary conditions are applied. At the sub-domain interfaces for the DSUG approach, no interpolation is required. At the slip boundary between the moving grid and stationary grid for the PSUG approach, conservative variables are interpolated based on arc lengths as in Ref. 9.

Results and Discussions

Two cases of flow simulation are presented here. The first simulation assumes inviscid flow, and the calculations are carried out using both DSUG and PSUG approaches. For viscous computation however, there will be large grid discontinuity across the slip boundary in the PSUG approach. Although the interpolation procedure across this boundary is conservative, the PSUG approach will not be adequate for the prediction of the unsteady wake flow. Hence only the DSUG approach is employed for simulating the physics of dynamic stall. The results for each case are obtained by starting from a converged steady solution at zero angle of attack. The airfoil is pitched up about its quarter-chord point. The pitching rate is prescribed in terms of "reduced frequency", κ , defined as

$$\kappa = \frac{\dot{\alpha}c}{V_{\infty}}$$

where $\dot{\alpha}$ is the angular velocity, c is the airfoil chord length, and V_{∞} is the freestream velocity.

Case 1: $M_{\infty} = 0.611$, $\kappa = 0.01492$

The airfoil is pitched up from 0° to 15° . Table 1 shows a summary of number of grid points (or cells) for each domain corresponding to the DSUG and PSUG approaches shown in Fig. 3. It should be noted that the number of cells and node points for the unstructured grid region are not the same for the two approaches. This is because there is a circular slip boundary in the PSUG approach but not in the DSUG approach.

Identical solutions are obtained using PSUG and DSUG approaches. Figure 4 shows the normal force coefficient vs. angle of attack for both numerical results and experimental data. Numerical results include both simulations with wind-tunnel wall and without wall assumption. Experimental data include the dynamic pitch-up as well as quasi-static measurements. These data indicate a quasi-static stall angle of attack (α_{qs}) at 2° earlier than the dynamic-stall angle of attack ($\alpha_d = 10.4^{\circ}$). It can be seen that before the dynamic stall ($\alpha < \alpha_d$), solutions without wall effect show very good agreement with the experimental data while those with wall effect differ from the experimental data up to 15 % (maximum at $\alpha = \alpha_d$). The good agreement is expected, since before the flow separates from the leading edge it is essentially inviscid.

Although identical solutions are obtained, the applications of the PSUG and DSUG approaches differ in the following aspects. The coding for the PSUG approach is less complex than for the DSUG approach. The stationary part of the unstructured grid for the PSUG

approach does not require computation of new metrics at each step. The only extra work in addition to updating the inner grid is interpolation along the slip boundary. For the DSUG approach, the unstructured grid is computed each time as the angle of attack is updated requiring additional memory for the transient data and metrics. The number of steps required in sub-iterations (such that $\hat{Q}^l \rightarrow \hat{Q}^{n+1}$) for the DSUG approach is between 20% to 30% less than for the PSUG approach. However, the CPU time required for the DSUG approach for the whole pitch-up history is at least one third more than that for the PSUG approach. This can be attributed to the grid updating and metrics computation at each angle of attack for the DSUG approach.

Case 2: $M_\infty = 0.3, Re = 2.7 \times 10^6, \kappa = 0.01492$

For resolving the unsteady boundary layer, the C grid around the airfoil is refined to include 141×31 grid points. The unstructured grid contains 1190 cells and 733 nodes. The other structured grids are same as the inviscid grids. The numerical computation is carried out up to $\alpha = 30^\circ$, while experimental data are only available from $\alpha = 0^\circ$ to $\alpha = 15^\circ$.

Pressure coefficient distribution snapshots are presented in Figs. 5a–5l. Excellent agreement with the experimental data can be seen for angle of attack up to 15.54° . This is true for approximations both with wall effect and without wall effect. As the angle of attack is increased to greater than 16.45° (Figs. 5f–5l), a significant difference is noticed between the leeward (upper surface) C_p of the with-wall and without-wall approximations. At $\alpha = 17.3^\circ$ (Fig. 5h), the leeward C_p of the with-wall approximation near the leading-edge becomes more positive and a local maximum (drop) and minimum (peak) are observed at $x/c = 0.04$ and 0.12 respectively. This suggests a leading-edge separation for the with-wall data. A similar curve is observed for the without-wall case in Fig. 5i. Moreover, the overall C_p distributions for the without-wall approximation evolve similarly to those of the with-wall approximation as the angle of attack increases (Figs. 5h – 5l) except they are slightly delayed.

For both the with-wall and without-wall approximations, it is seen that the peak in leeward C_p (started in Fig. 5h or 5i) moves downstream as the angle of attack increases. It is also shown in Figs. 5h–5l that the peaks in leeward C_p distribution result in a larger overall difference in windward and leeward curves comparing to those of $\alpha = 16.45^\circ$ (Fig. 5g). This clearly indicates that there is an increase in lift (net area of C_p distribution) after the leading edge separation. However, it is observed in Figs. 6a–6f that as the peaks of the leeward C_p move close to the trailing edge, the net area becomes less. In particular, at

$\alpha > 25.05^\circ$, these peaks are hardly noticeable.

The phenomena observed in the C_p distribution plots are also demonstrated in Fig. 7, the history of the normal force coefficient. In this plot, both approximations (with wall and without wall) are plotted for angle of attack up to 30° . For the range $\alpha < 15^\circ$ where experimental data are available, it can be seen that there is a good agreement between the measurements and the numerical data. In addition to predicting the linear relationship between C_n and α , the with-wall approximation is shown to be closer to the experimental data than the without-wall approximation. Most importantly, both of the numerical approximations show significant overshoots of the normal force coefficient (comparing to the quasi-static C_n maximum) at angle of attack after the leading edge separation has occurred. This maximum C_n is 2.3, 64% greater than the quasi-static value. The angle at which the maximum C_n occurs is 21.5° (without wall), which is 6.5° higher than the α_{qs} . That is, the dynamic pitch-up allows a 6.5° margin after the quasi-static stall angle and it yields an additional 64% normal force coefficient. It is also interesting to note that up to 5° after the dynamic stall, both approximations (with and without wall) exhibit similar features except one lags the other by a maximum of 2° .

Figure 8 shows a sequence of plots of density contours for the with-wall approximation ranging from $\alpha = 16.45^\circ$ to 29.05° . It can be seen that after the leading edge separation (Fig. 8b), a vortex develops at the leading edge (shown by concentric contour levels in Fig. 8c, $\alpha = 18.2^\circ$). This vortex moves downstream and becomes bigger as the angle of attack increases (Figs. 8c-8f). It is also referred to as the leading edge vortex in dynamic stall. As the leading edge vortex reaches the vicinity of the trailing edge (Fig. 8g), it is seen to interact with a newly developed trailing edge vortex. This phenomenon is first observed at $\alpha = 22^\circ$, an angle of attack close to the dynamic stall. In Figs. 8h-8l, the trailing edge vortex is seen to become bigger and the leading edge vortex more diffused. Eventually this vortex system moves downstream from the trailing edge (Fig. 8j). In Fig. 8k ($\alpha = 26.1^\circ$), another vortex is developed at the trailing edge and the same process described above is seen to repeat (Fig. 8l). It should be mentioned that there are other small vortices observed in the sequence of plots. However, we only concentrate on the main features which govern the flow behavior.

As mentioned in the introduction, our numerical solutions will be used to predict the wall effect and compared to the PIDV flow field measurements. In addition to the data shown here, other flow properties are readily extracted from these solutions. Ultimately,

the numerical simulation and experimental measurements will compliment each other in analyzing and understanding dynamic stall.

Conclusion

A hybrid-grid Navier-Stokes approach is developed to study dynamic stall over an airfoil including wind tunnel wall effect. Although it takes more CPU time in grid updating, the DSUG approach is more efficient than the PSUG approach in sub-iterations convergence. Good agreement is obtained between solutions and available experimental data. The unsteady vortical flow phenomena are captured and they provide insight into the physics associated with dynamic stall.

Acknowledgement

This work is supported by the Supercomputer Computations Research Institute at the Florida State University, which is partially supported by the US Department of Energy under the contract number DE-FC05-85ER250000.

References

- ¹ Shih, C., Lourenco, L., and Krothapalli, A., "PIDV: An Integrated Tool for the Measurement of Unsteady Separated Flows," *ASME Symposium on Non-Steady Viscous Flows*, June 1990.
- ² Landon, R.H., "NACA0012 Oscillatory and transient pitching," *Compendium of Unsteady Aerodynamic Measurements*, AGARD Report No.702.
- ³ McCroskey, W. J., McAlister, K. W., Carr, L. W., Pucci, S. L., Lambert, O., and Idergand, R. F., "Dynamic Stall on Advanced Airfoil Sections," *J. of American Helicopter Society*, July 1981, pp. 40-50
- ⁴ Visbal, M.R., "Effect of Compressibility on Dynamic Stall of a Pitching Airfoil," AIAA Paper No. 88-0132, Jan. 1988.
- ⁵ Carr, L.W., Chandrasekhara, M., Ahmed, S., and Brock, N., "A Study of Dynamic Stall Using Real Time Interferometry," AIAA Paper No. 91-0007, Jan. 1991.
- ⁶ Lohner, R., "Adaptive Remeshing for Transient Problems," *Computer Methods in Applied Mechanics and Engineering*, Vol. 75, 1989, pp. 195-214.

- ⁷ Thomas, J.L., Walters, R.W., Reu, T., Ghaffari, F., Weston, R.P., and Luckring, J.M., "A Patched-Grid Algorithm for Complex Configurations Directed towards the F/A-18 Aircraft," AIAA Paper 89-0121, Jan. 1989.
- ⁸ Meakin, R.L. and Suhs, N.E., "Unsteady Aerodynamic Simulation of Multiple Bodies in Relative Motion," AIAA Paper 89-1996-CP, June, 1989.
- ⁹ Rai, M.M., "Unsteady Three-Dimensional Navier-Stokes Simulations of Turbine Rotor-Stator Interaction," AIAA Paper 87-2058, June 1987.
- ¹⁰ Thomas, J.L. and Walters, R.W., "Upwind Relaxation Algorithms for the Navier Stokes Equations," AIAA Paper 85-1501, July, 1985.
- ¹¹ Roe, P.L., "Characteristic Based Schemes for the Euler Equations," *Ann. Rev. Fluid Mech.*, Vol. 18, 337-365 (1986) .
- ¹² Holst, T.L., Kaynak, U., Gundy, K.L., Thomas, S.D., Florest, J., and Chaderjian, N.M., "Transonic Wing Flows Using Euler/Navier-Stokes Zonal Approach", *Journal of Aircraft*, Vol. 24, No.1, pp.17-24.
- ¹³ Baldwin, B.S. and Lomax, H., "Thin-Layer Approximation and Algebraic Model for Separated Turbulent Flows," AIAA Paper 78-257.
- ¹⁴ Anderson, W.K., Thomas, J.L., and Van Leer, B., "A Comparison of Finite Volume Flux Vector Splitting for the Euler Equations," AIAA Paper 85-0122, Jan. 1985.
- ¹⁵ Reu, T. and Ying, S.X., "An Adaptive Multi-Coloring Scheme for Solving the Euler Equations on Unstructured Grids," *Proceedings of the Third International Conference on Numerical Grid Generation in CFD and Related Fields*, June 1991, pp.391-402.
- ¹⁶ Steger, J.L. and Sorenson, R.L., "Automatic Mesh-Point Clustering Near a Boundary in Grid Generation with Elliptic Partial Differential Equations," *Journal of Computational Physics*, Vol. 33, 1979, pp.405-410.
- ¹⁷ Sloan, S.W., "A Fast Algorithm for Constructing Delaunay Triangulations in the Plane," *Adv. Eng. Software*, 1987, Vol. 9, No.1, pp.34-55.
- ¹⁸ Mavriplis, D.J., "Adaptive Mesh Generation for Viscous Flows Using Delaunay Triangulation," *Proceedings of the Numerical Grid Generation in CFD and Related Fields*, 1988, pp.611-620.
- ¹⁹ Batina, J.T., "Three-Dimensional Flux-Split Euler Schemes Involving Unstructured Dynamic Meshes," AIAA Paper 90-1649, June, 1990.

Figure Captions

Fig. 1 A Comparison of the hybrid grid approaches at $\alpha = 3.82^\circ$

- a) Details of an inviscid grid around the airfoil for the PSUG approach.
- b) Details of an inviscid grid around the airfoil for the DSUG approach.

Fig. 2 Variables definition on the unstructured grid.

Fig. 3 Sub-domains of grid topology

- a) The PSUG topology.
- b) The DSUG topology.

Fig. 4 Normal force coefficient hysteresis vs. angle of attack for inviscid flow simulation at $M_\infty = 0.611$ and $\kappa = 0.01492$.

Fig. 5 Surface pressure coefficients distribution before dynamic stall at

$M_\infty = 0.3, Re = 2.7 \times 10^6$, and $\kappa = 0.02546$.

- a) $\alpha = 0^\circ$
- b) $\alpha = 2.94^\circ$
- c) $\alpha = 5.84^\circ$
- d) $\alpha = 8.91^\circ$
- e) $\alpha = 11.76^\circ$
- f) $\alpha = 15.54^\circ$
- g) $\alpha = 16.45^\circ$
- h) $\alpha = 17.3^\circ$
- i) $\alpha = 18.2^\circ$
- j) $\alpha = 19.51^\circ$
- k) $\alpha = 20.91^\circ$
- l) $\alpha = 21.9^\circ$

Fig. 6 Surface pressure coefficients distribution after dynamic stall at

$M_\infty = 0.3, Re = 2.7 \times 10^6$, and $\kappa = 0.02546$.

- a) $\alpha = 23.0^\circ$
- b) $\alpha = 24.06^\circ$
- c) $\alpha = 25.2^\circ$
- d) $\alpha = 26.07^\circ$
- e) $\alpha = 27.04^\circ$
- f) $\alpha = 29.05^\circ$

Fig. 7 Normal force coefficient hysteresis vs. angle of attack for dynamic stall simulation at $M_\infty = 0.3$, $Re = 2.7 \times 10^6$, and $\kappa = 0.02546$.

Fig. 8 Density contours of the dynamic stall at $M_\infty = 0.3$, $Re = 2.7 \times 10^6$, and $\kappa = 0.02546$.

- a) $\alpha = 16.45^\circ$
- b) $\alpha = 17.33^\circ$
- c) $\alpha = 18.2^\circ$
- d) $\alpha = 19.51^\circ$
- e) $\alpha = 20.91^\circ$
- f) $\alpha = 21.96^\circ$
- g) $\alpha = 23.0^\circ$
- h) $\alpha = 24.06^\circ$
- i) $\alpha = 25.2^\circ$
- j) $\alpha = 26.07^\circ$
- k) $\alpha = 27.04^\circ$
- l) $\alpha = 29.05^\circ$

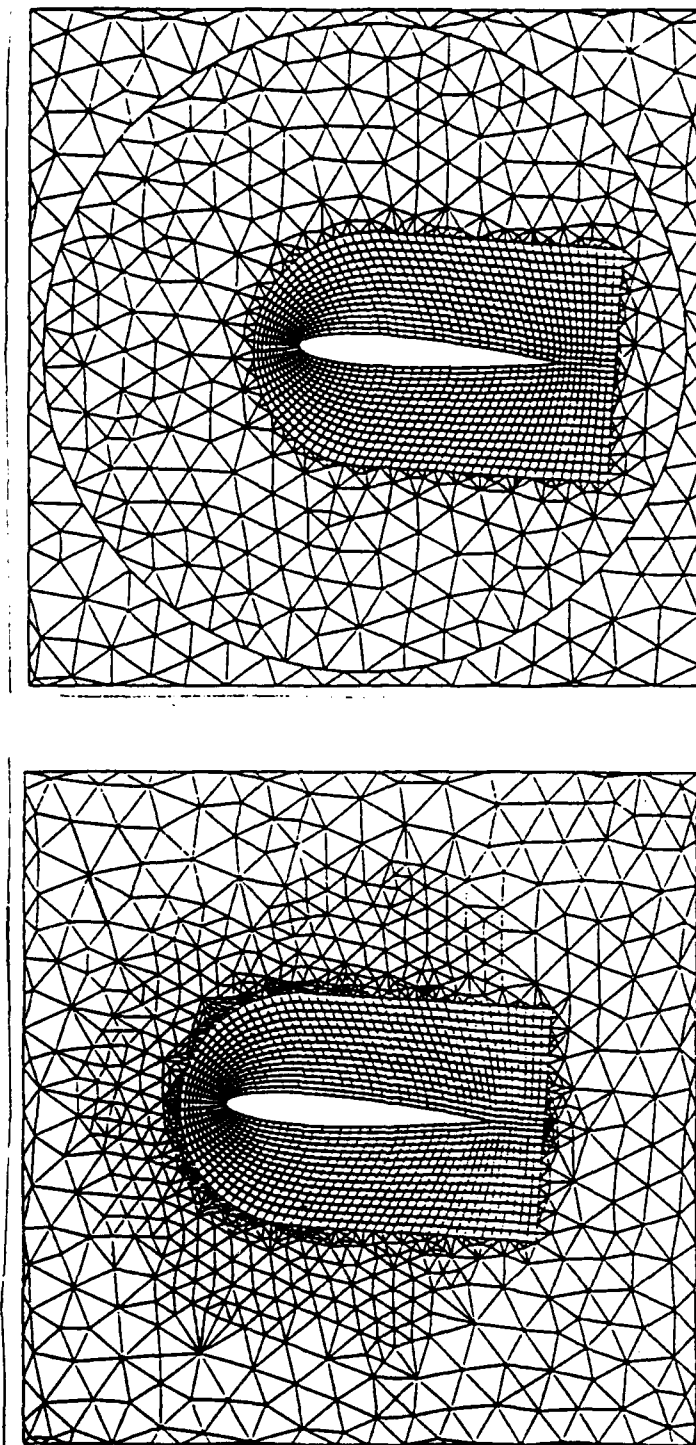


Fig. 1 A Comparison of the hybrid grid approaches at $\alpha = 3.82^\circ$

- a) Details of an inviscid grid around the airfoil for the PSUG approach.**
- b) Details of an inviscid grid around the airfoil for the DSUG approach.**

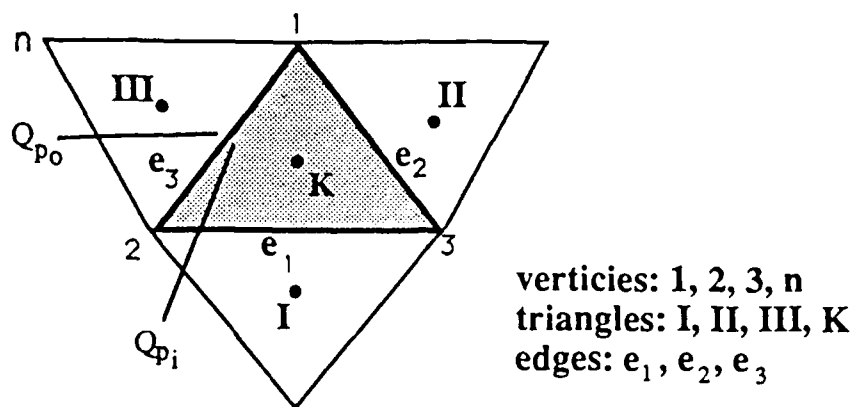


Fig. 2 Variables definition on the unstructured grid.

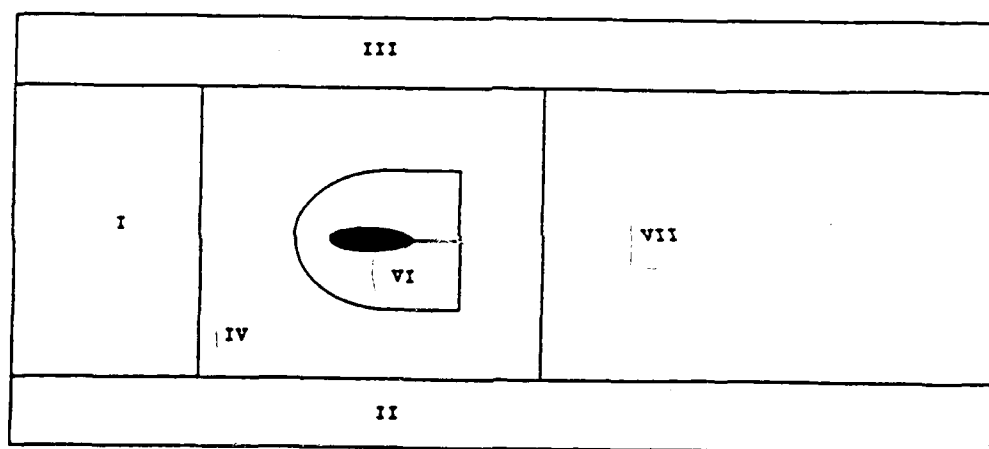
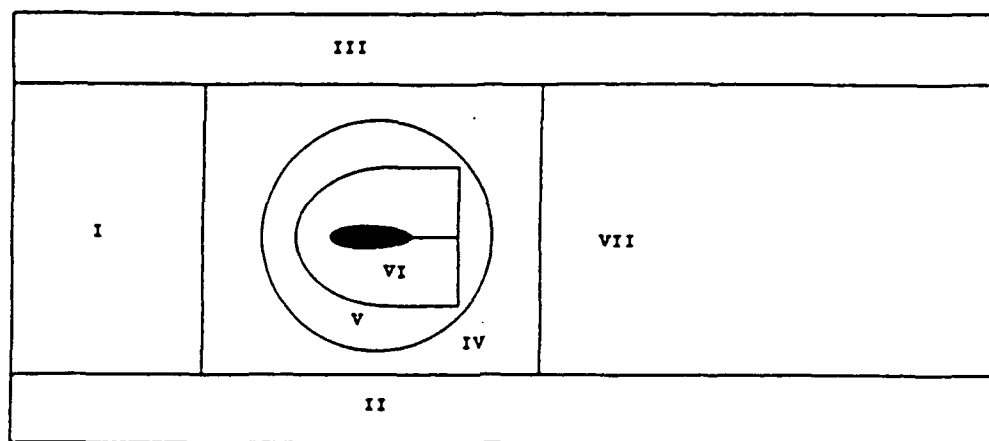


Fig. 3 Sub-domains of grid topology

a) The PSUG topology.

b) The DSUG topology.

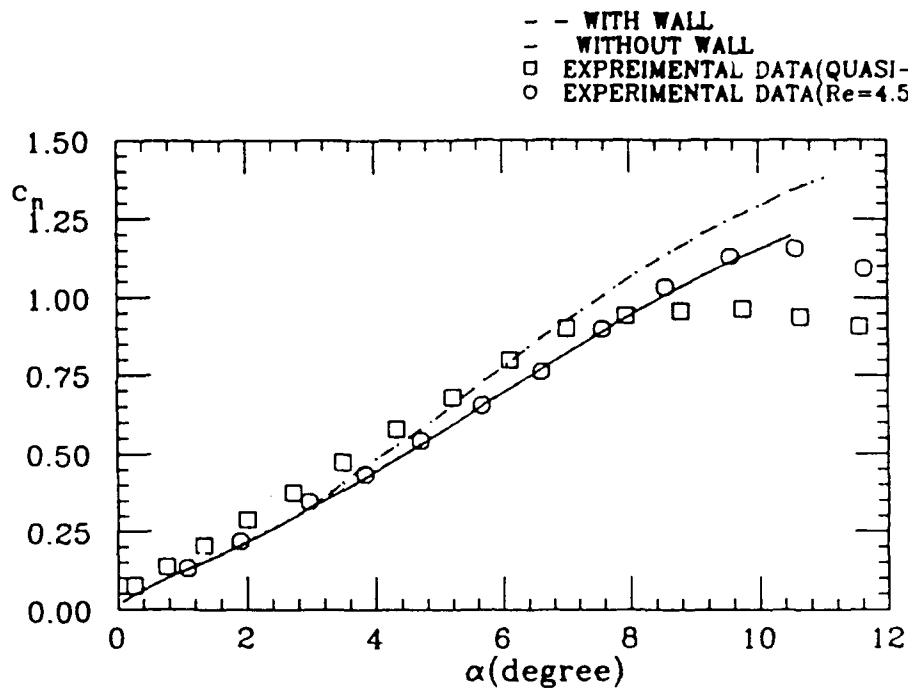
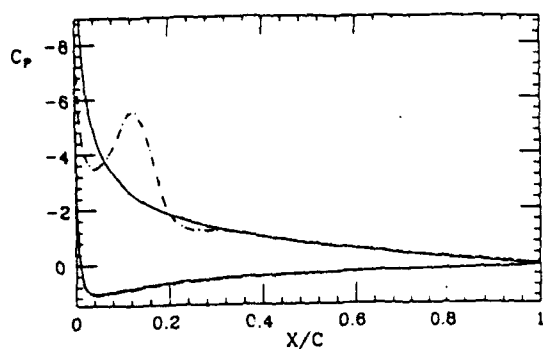
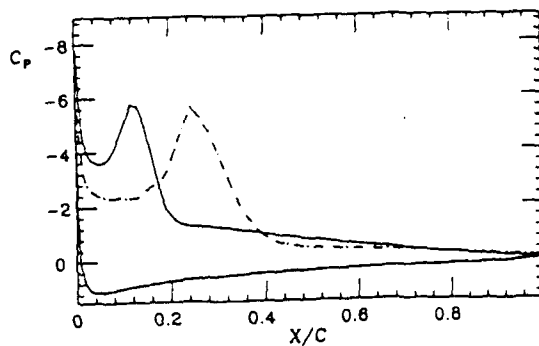


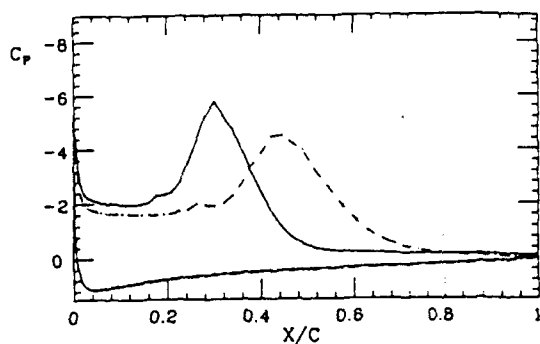
Fig. 4 Normal force coefficient hysteresis vs. angle of attack for inviscid flow simulation at $M_\infty = 0.611$ and $\kappa = 0.01492$.



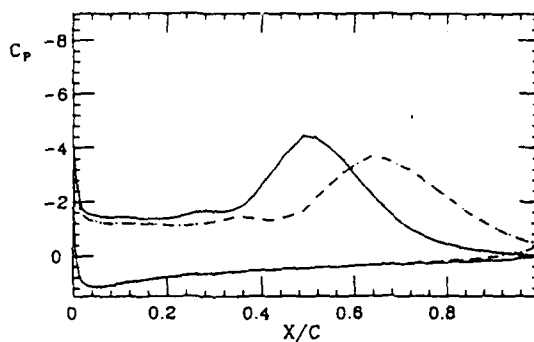
(h) $\alpha = 17.3^\circ$



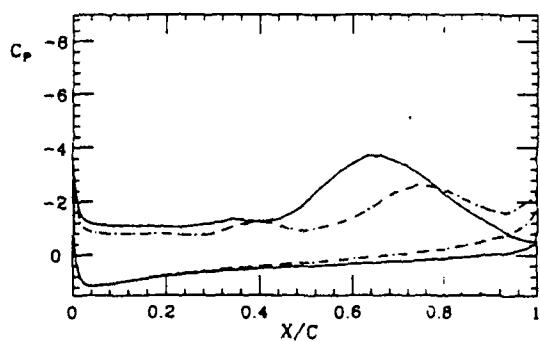
(i) $\alpha = 18.2^\circ$



(j) $\alpha = 19.51^\circ$



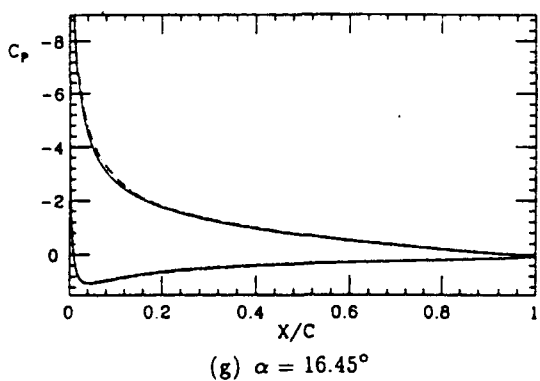
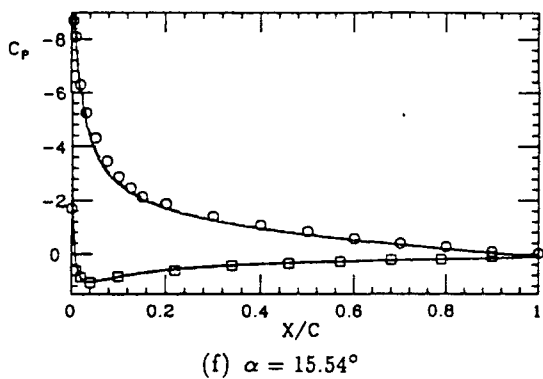
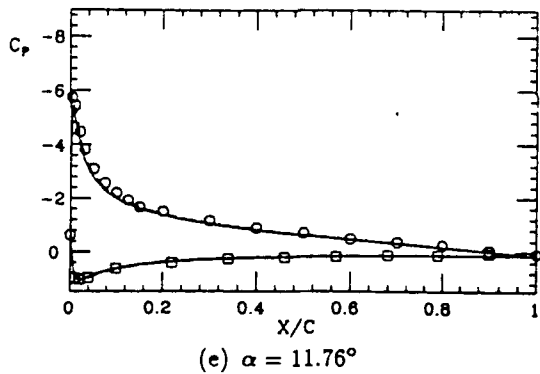
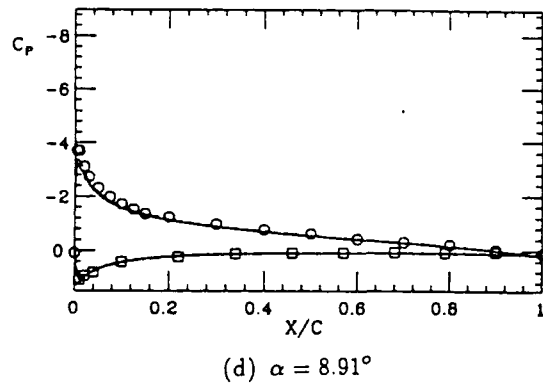
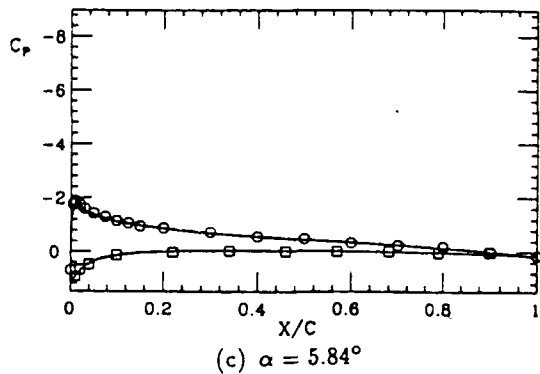
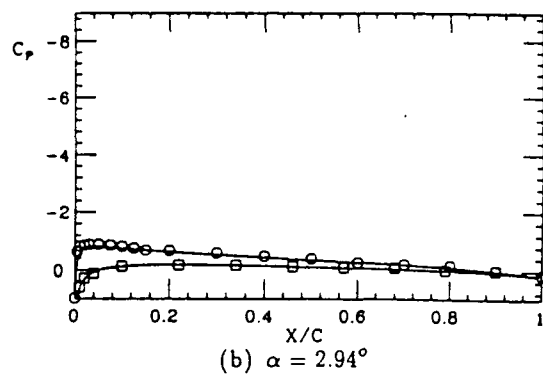
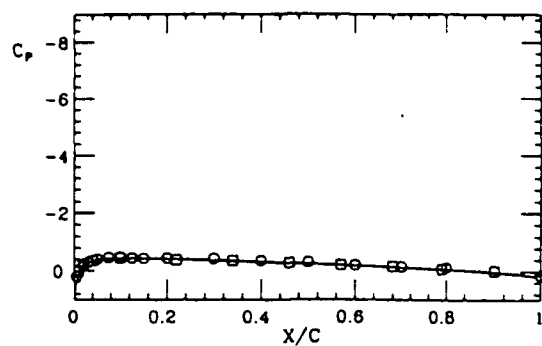
(k) $\alpha = 20.91^\circ$



(l) $\alpha = 21.9^\circ$

- - WITH WALL
 - - WITHOUT WALL
 ○ EXPERIMENTAL DATA(TOP)
 □ EXPERIMENTAL DATA(BOTTOM)

Figure 5 Surface pressure coefficients distribution for viscous flow
at $M_\infty = 0.3$, $Re = 2.7 \times 10^6$, and $\kappa = 0.02546$.



- - WITH WALL
 - - WITHOUT WALL
 O EXPERIMENTAL DATA(TOP)
 □ EXPERIMENTAL DATA(BOTTOM)

Figure 5 Surface pressure coefficients distribution for viscous flow
at $M_\infty = 0.3$, $Re = 2.7 \times 10^6$, and $\kappa = 0.02546$. (continued)

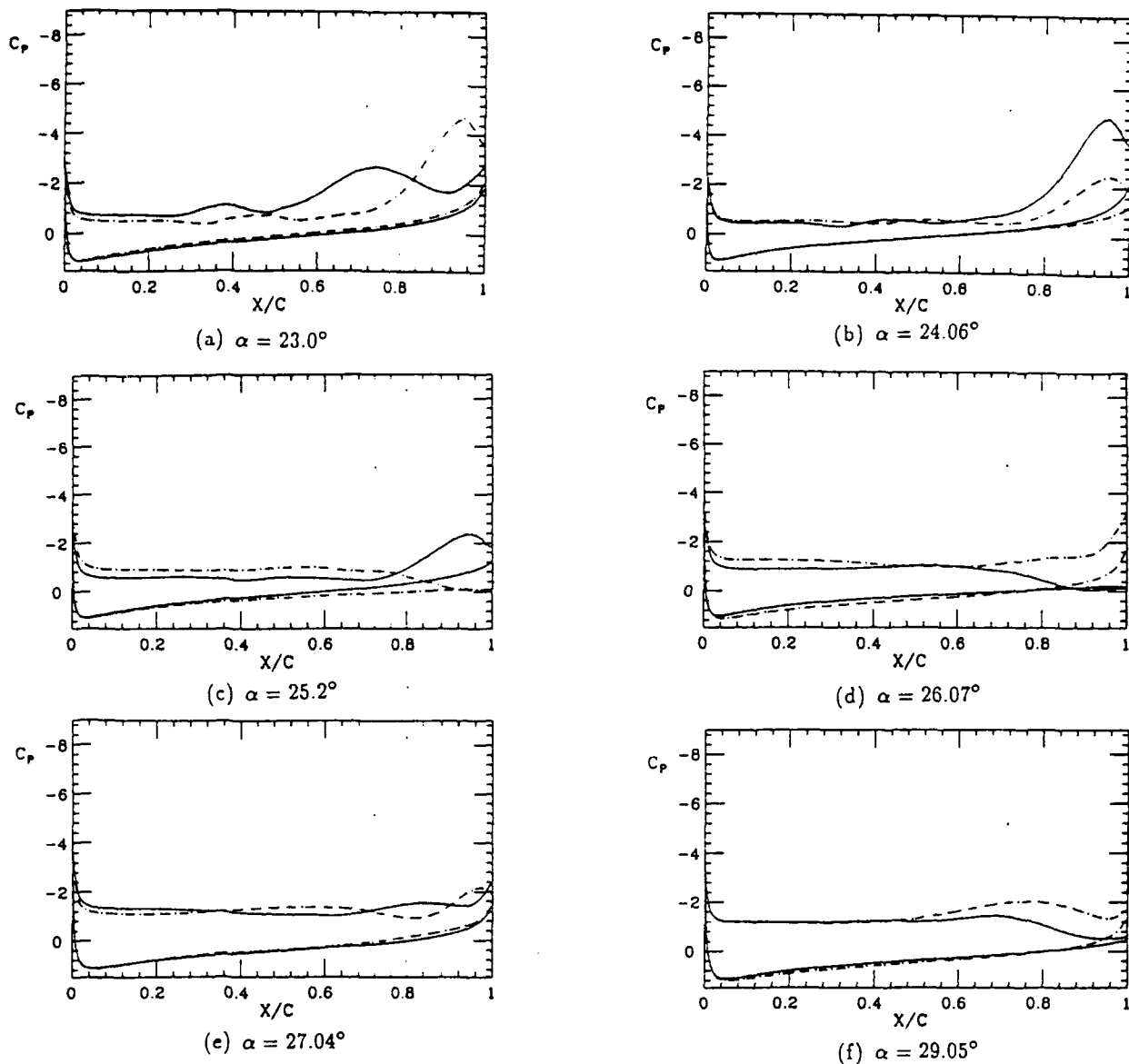


Figure 6 Surface pressure coefficients distribution after dynamic stall at $M_\infty = 0.3$, $Re = 2.7 \times 10^6$, and $\kappa = 0.02546$.

NACA0012 AIRFOIL ($M_\infty=0.3$ $\omega c/v=0.02545$)
TLNS (DYNAMIC GRID)

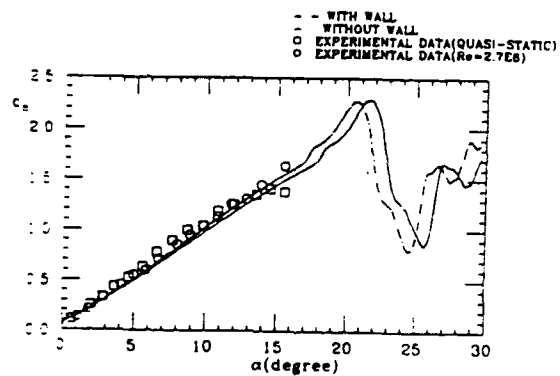
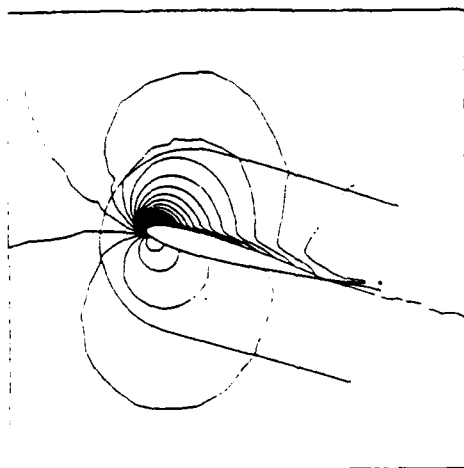
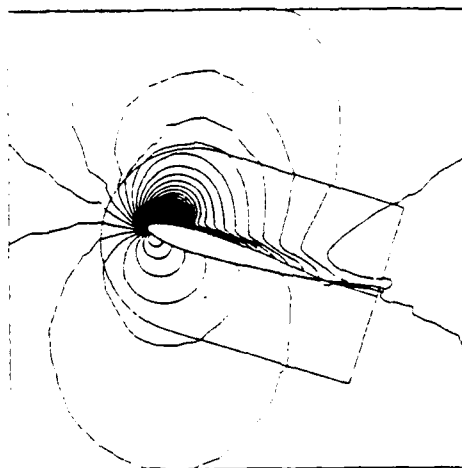


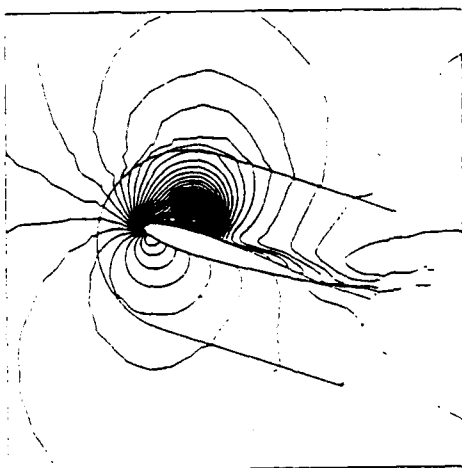
Figure 7 Normal force coefficient hysteresis vs. angle of attack for turbulent flow at $M_\infty = 0.3$, $Re = 2.7 \times 10^6$, and $\kappa = 0.02546$.



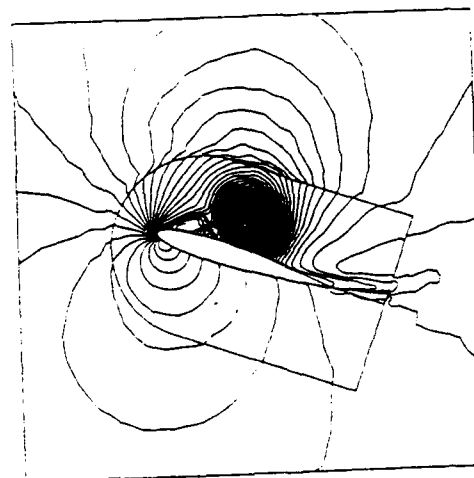
(a) $\alpha = 16.45^\circ$



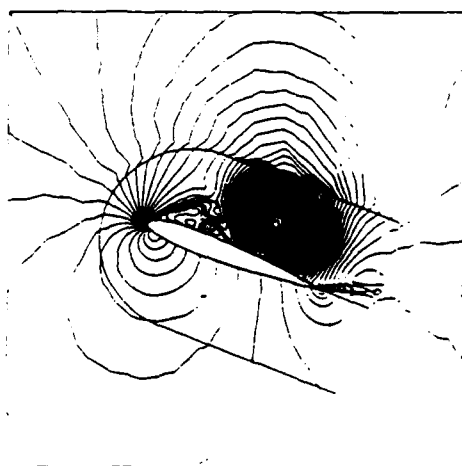
(b) $\alpha = 17.33^\circ$



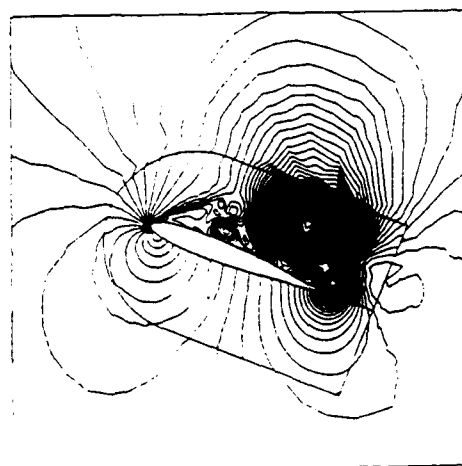
(c) $\alpha = 18.2^\circ$



(d) $\alpha = 19.51^\circ$

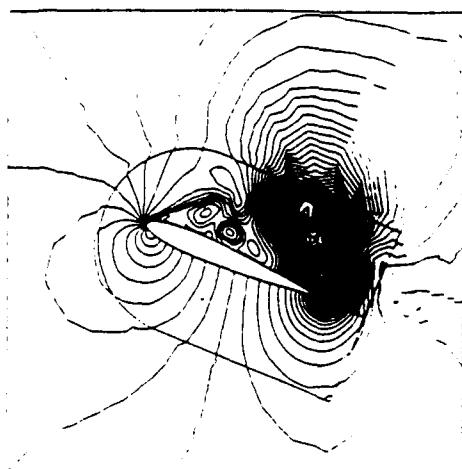


(e) $\alpha = 20.91^\circ$

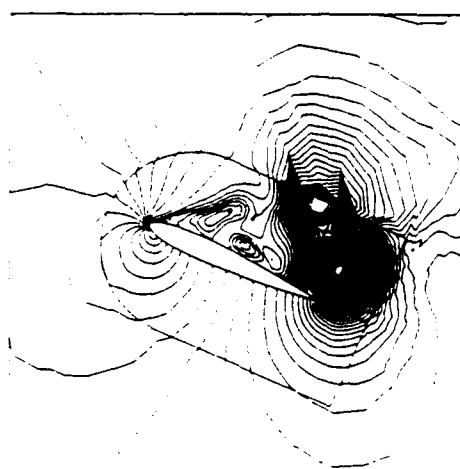


(f) $\alpha = 21.96^\circ$

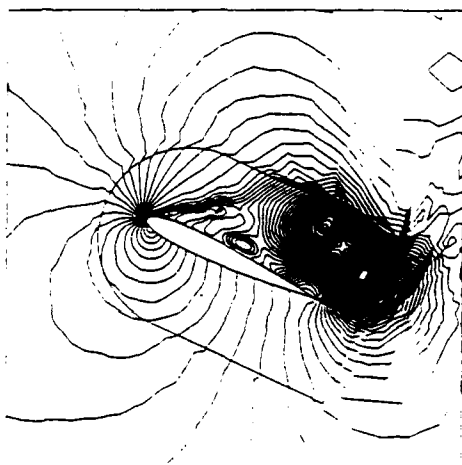
Figure 8 Density contours of the with-wall case at $M_\infty = 0.3$, $Re = 2.7 \times 10^6$, and $\kappa = 0.02546$. (continued)



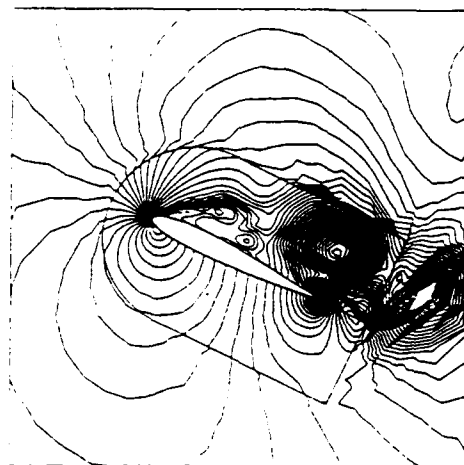
(g) $\alpha = 23.0^\circ$



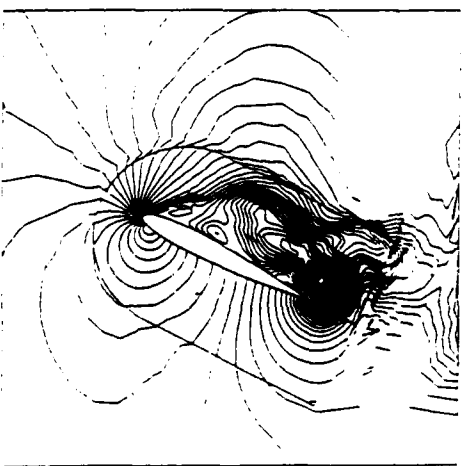
(h) $\alpha = 24.06^\circ$



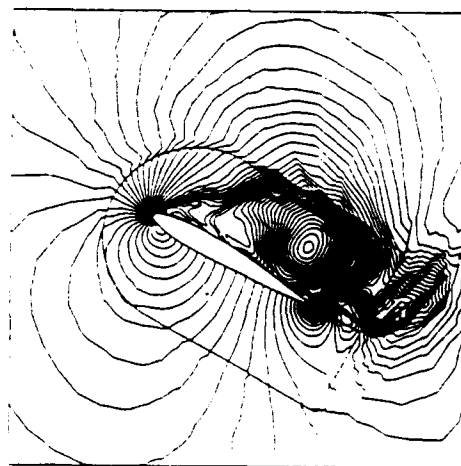
(i) $\alpha = 25.2^\circ$



(j) $\alpha = 26.07^\circ$



(k) $\alpha = 27.04^\circ$



(l) $\alpha = 29.05^\circ$

Figure 8 Density contours of the with-wall case at $M_\infty = 0.3$, $Re = 2.7 \times 10^6$, and $\kappa = 0.02546$.

Table 1 Number of grid points and cells in each sub-domain

	I	II	III	IV	V	VI	VII
PSUG	24x19	101x7	101x7	398 cells, 262 nodes	694cells, 433 nodes	95x15	58x19
DSUG	24x19	101x7	101x7	1838 cells, 1018nodes	0	95x15	58x19